

# Mechanical forces switch blood vessel subtypes to arrest adolescent bone growth

**Max Löhning** (✉ [max.loehning@charite.de](mailto:max.loehning@charite.de))

Charite - University Medicine Berlin <https://orcid.org/0000-0001-6382-7281>

**Maria Dzamukova**

German Rheumatism Research Center (DRFZ)

**Tobias Brunner**

German Rheumatism Research Center (DRFZ)

**Jadwiga Miotla-Zarebska**

Kennedy Institute of Rheumatology

**Frederik Heinrich**

German Rheumatism Research Centre (DRFZ) Berlin

**Laura Brylka**

University Medical Center Hamburg - Eppendorf <https://orcid.org/0000-0003-4734-9966>

**Mir-Farzin Mashreghi**

Deutsches Rheuma-Forschungszentrum Berlin <https://orcid.org/0000-0002-8015-6907>

**Anjali Kusumbe**

University of Oxford <https://orcid.org/0000-0002-1911-5495>

**Ralf Kuehn**

Max Delbrück Center for Molecular Medicine <https://orcid.org/0000-0003-1694-9803>

**Thorsten Schinke**

University Medical Center Hamburg-Eppendorf

**Tonia Vincent**

Kennedy Institute of Rheumatology

---

## Biological Sciences - Article

**Keywords:** bone growth, vessels

**Posted Date:** January 12th, 2021

**DOI:** <https://doi.org/10.21203/rs.3.rs-120475/v1>

**License:**   This work is licensed under a Creative Commons Attribution 4.0 International License.

[Read Full License](#)

---

**Version of Record:** A version of this preprint was published at Nature Communications on June 1st, 2022.  
See the published version at <https://doi.org/10.1038/s41467-022-30618-8>.

1 **Mechanical forces switch blood vessel subtypes to arrest adolescent bone growth**

2 Maria Dzamukova<sup>1,2</sup>, Tobias M. Brunner<sup>1,2</sup>, Jadwiga Miotla-Zarebska<sup>3</sup>, Frederik Heinrich<sup>4</sup>,  
3 Laura Brylka<sup>5</sup>, Mir-Farzin Mashreghi<sup>4,6</sup>, Anjali Kusumbe<sup>7</sup>, Ralf Kühn<sup>8</sup>, Thorsten Schinke<sup>5</sup>,  
4 Tonia L. Vincent<sup>3</sup>, Max Löhning<sup>1,2\*</sup>

5  
6 **Affiliations**

7 <sup>1</sup> Pitzer Laboratory of Osteoarthritis Research, German Rheumatism Research Centre (DRFZ), a  
8 Leibniz Institute, Berlin, Germany.

9 <sup>2</sup> Department of Rheumatology and Clinical Immunology, Charité - Universitätsmedizin Berlin,  
10 corporate member of Freie Universität Berlin, Humboldt-Universität zu Berlin and Berlin Institute of  
11 Health, Berlin, Germany.

12 <sup>3</sup> Centre for Osteoarthritis Pathogenesis Versus Arthritis, Kennedy Institute of Rheumatology,  
13 University of Oxford, Oxford, United Kingdom.

14 <sup>4</sup> Therapeutic Gene Regulation, Regine von Ramin Lab Molecular Rheumatology, German  
15 Rheumatism Research Centre (DRFZ), a Leibniz Institute, Berlin, Germany.

16 <sup>5</sup> Department of Osteology and Biomechanics, University Medical Centre Hamburg-Eppendorf,  
17 20246 Hamburg, Germany.

18 <sup>6</sup> BCRT/DRFZ Single-Cell Laboratory for Advanced Cellular Therapies – Berlin-Brandenburg Centre  
19 for Regenerative Therapies (BCRT), Berlin, Germany.

20 <sup>7</sup> Tissue and Tumour Microenvironments Group, Kennedy Institute of Rheumatology, University of  
21 Oxford, Oxford, United Kingdom.

22 <sup>8</sup> Max Delbrück Centre for Molecular Medicine, Berlin, Germany.

23 \* Correspondence: max.loehning@charite.de

1 **Abstract**

2 Bone growth requires a specialised, highly angiogenic blood vessel subtype, so-called type H  
3 vessels<sup>1,2</sup>, which pave the way for osteoblasts surrounding these vessels<sup>3</sup>. At the end of  
4 adolescence, type H endothelial cells differentiate into quiescent type L endothelium lacking  
5 the capacity to promote bone growth. Until now, the signals that switch off type H vessel  
6 identity and thus arrest adolescent bone growth have remained ill defined. Here we show that  
7 mechanical forces, associated with increased body weight at the end of adolescence, trigger the  
8 mechanoreceptor PIEZO1 and thereby mediate enhanced production of the kinase FAM20C in  
9 osteoblasts. FAM20C phosphorylates dentin matrix protein 1 (DMP1)<sup>4</sup>, previously identified  
10 as a key factor in bone mineralization<sup>5</sup>. This phosphorylation elicits a burst in DMP1 secretion  
11 from osteoblasts. Extracellular DMP1 inhibits vascular endothelial growth factor (VEGF)  
12 signalling by preventing VEGFR2 phosphorylation and VEGFR3 expression on the tip cells of  
13 type H endothelium. DMP1-mediated VEGF inhibition transforms bone growth-promoting  
14 type H vessels into quiescent type L vasculature to arrest bone growth and enhance bone  
15 mineralization. This molecular mechanism links mechanical forces and the termination of bone  
16 growth via accumulation of an extracellular matrix protein and its regulation of vascular  
17 subtypes. It suggests new options for the treatment of diseases characterised by inappropriate  
18 turnover or invasion of bone such as osteoarthritis, osteoporosis and osteosarcoma.

19

## 1 **DMP1 is a potential candidate controlling endothelial cell fate in bone**

2 To dissect age-related changes in vascular and perivascular microenvironments during and after active  
3 bone growth, we performed laser microdissection (LMD) of single capillary with associated  
4 surrounding cells in the ossification front (OF) of juvenile (4-week-old) and adult (12-week-old) mice.  
5 We developed a protocol to cut single capillary from undecalcified and unfixed bones of endothelial  
6 cell-specific GFP-reporter mice with a high RNA preservation rate to subsequently perform next-  
7 generation sequencing (NGS) (Extended Data Fig. 1a,b). Principal component analysis showed that the  
8 cells from the juvenile OF were very similar between different mice, whereas with ageing, greater  
9 heterogeneity was apparent (Extended Data Fig. 1c). To identify candidates from the list of  
10 differentially expressed genes with a potential of regulating type H vasculature, we focused on  
11 extracellular matrix (ECM) proteins (Fig. 1a and Extended Data Fig. 1d). DMP1 appeared to be a  
12 promising candidate because of its ~4-fold higher expression in juvenile bones (Fig. 1a,b) and its  
13 reported anti-angiogenic activity in a retina tumour model<sup>6</sup>.

14 DMP1 is known as an essential player in matrix mineralization<sup>5,7</sup>. Our detailed analysis of DMP1  
15 protein localization throughout postnatal bone development showed that until 5 weeks of age, the  
16 protein was mainly localized at the base of the zone of type H vessels in the OF (Fig. 1c,d).  
17 Unexpectedly, at the age of 5.5-6 weeks, a burst in DMP1 secretion into ECM occurred primarily in the  
18 central top part of the OF also reaching the growth plate (GP) (Fig. 1c,e-g and Extended Data Fig. 2a).  
19 We performed automated quantifications of protein staining intensities within central and peripheral  
20 regions of interest in the OF (Fig. 1f,g and Extended Data Fig. 2b). During late postnatal bone  
21 maturation with increasing age, the DMP1-occupied area spread from the centre towards the periphery  
22 of the OF. Finally, by the age of 12 weeks, the whole metaphysis together with the GP were interspersed  
23 with DMP1 (Fig. 1c,f,g). This behaviour was seen irrespective of sex.

24 To identify the main cellular source of DMP1 in the OF-GP area at different ages, we established a  
25 method for RNAScope in bone. Co-hybridization was performed with probes for *Dmp1* together with  
26 *Runx2* for early osteoblasts, osterix (*Osx* or *Sp7*) for mature osteoblasts<sup>1</sup> and sclerostin (*Sost*) for  
27 osteocytes<sup>8</sup> (Extended Data Fig. 2c). Sclerostin expression was not found in the OF. At all analysed  
28 stages, *Dmp1* mRNA was only detected in the OF area but never in the chondrocytes of the GP,

1 including time points directly before (5 weeks) and during the burst in DMP1 protein secretion (5.5  
2 weeks) (Fig. 1h and Extended Data Fig. 2f). *Dmp1* mRNA was mainly found in *Osx*<sup>+</sup> cells and to a  
3 lesser extent in *Runx2*<sup>+</sup> cells at all examined time points, which identifies osteoblasts as the main  
4 producer of DMP1 in the metaphysis (Extended Data Fig. 2d,e). The number and intensity of *Dmp1*-  
5 expressing cells peaked at 4-5 weeks (Fig. 2i,j and Extended Data Fig. 2g). Yet, there was no difference  
6 at the level of *Dmp1* gene expression between the central and peripheral parts of the OF, indicating that  
7 the observed differences in DMP1 amounts between these regions emerged rather at the protein level  
8 (cf. Fig. 1c,f,g). Together, these data demonstrate that the burst in DMP1 secretion from osteoblasts in  
9 the OF centre at the age of 5.5-6 weeks is controlled at the protein level and DMP1 likely diffuses from  
10 the OF to the GP (Fig. 1k).

11

## 12 **DMP1 transforms type H vessels into type L**

13 In addition to secreting osteogenic factors<sup>2</sup>, tip cells of type H vessels secrete matrix metalloproteinase  
14 9 (MMP9) that digests cartilage matrix and allows vessel bulges to invade GP cartilage, thereby  
15 facilitating bone growth<sup>9</sup>. We noticed that DMP1 accumulation in the OF centre at 5.5-6 weeks  
16 correlated with a decrease in endomucin (EMCN) intensity and reduced amounts of MMP9 at the OF-  
17 GP border. This was associated with the disappearance of bulges and columnar structure of the vessels  
18 (Fig. 2a,b, Extended Data Fig. 3). Hence, all main features of type H vessels were downregulated.  
19 Importantly, at 5.5-6 weeks, these changes occurred only in the central part of the OF.

20 To study whether DMP1 directly regulated bone angiogenesis and growth, we generated mice with a  
21 constitutive and an inducible deletion of *Dmp1* (Extended Data Fig. 4). Constitutive *Dmp1*-deficient  
22 mice were smaller with shortened and widened long bones (Extended Data Fig. 4c-f) as had been  
23 described before<sup>5,10</sup>, and they featured a disorganized OF and GP (Extended Data Fig. 5a). The blood  
24 vessels in the OF were dilated and had very high EMCN and MMP9 intensity, even in adulthood, though  
25 the columnar structure was lost already in juvenile bones (Extended Data Fig. 5c,d). This finding  
26 suggests that, presumably via its matrix mineralization activity, DMP1 provides a scaffold for columns  
27 of type H vessels. The phenotype of *Dmp1*<sup>+/-</sup> mice was identical to *Dmp1*<sup>+/+</sup> mice, which indicates that  
28 one *Dmp1* allele generates sufficient DMP1 protein (Extended Data Fig. 4c,d and 5b). This result is

1 consistent with human genetic studies where it was shown that mutations in the *Dmp1* gene cause  
2 autosomal recessive hypophosphatemia<sup>11</sup>. *OSX*<sup>+</sup> and *RUNX2*<sup>+</sup> osteoblasts were present in the OF to a  
3 similar extent as in the wild-type group indicating that DMP1 is not required for osteoblast  
4 differentiation and maturation<sup>12</sup> (Extended Data Fig. 5a,b). Notably, the GP of *Dmp1*<sup>-/-</sup> mice exhibited  
5 an expanded pre-hypertrophic and hypertrophic zone (*RUNX2*<sup>+</sup> and *SOX9*<sup>+</sup>) (Extended Data Fig. 5a).  
6 We assume that this phenotype is caused by the lack of proper vessel invasion due to the loss of vessel  
7 architecture.

8 To test whether DMP1 induces the switch from type H to type L vessels, we generated a *Dmp1*-floxed  
9 mouse line and crossed it with *Col1-CreERT2* mice to ablate *Dmp1* in an inducible manner selectively  
10 in osteoblasts (*Dmp1*<sup>iΔOB</sup>) upon tamoxifen injection (Extended Data Fig. 4g-i). Deletion of *Dmp1* was  
11 performed at P28-32 to allow normal formation of the OF together with the columnar structure of blood  
12 vessels (Fig. 2c). Tamoxifen treatment led to ~75% reduction of *Dmp1* mRNA expression by week 6  
13 (P42) (Extended Data Fig. 6a,b) and reduced the amount of DMP1 protein in the OF centre by ~70%  
14 (Fig. 2d and Extended Data Fig. 6c). The body weight was not affected (Extended Data Fig. 6d). Yet,  
15 long bones of *Dmp1*<sup>iΔOB</sup> mice featured an enlarged metaphysis with overall increased EMCN and  
16 MMP9 intensities (Fig. 2e,f and Extended Data Fig. 6e). In line with the femur phenotype of constitutive  
17 *Dmp1*-deficient mice (cf. Extended Data Fig. 4d,f), also *Dmp1*<sup>iΔOB</sup> femurs were slightly shorter than  
18 control femurs by the age of 6 weeks, presumably reflecting the key role of DMP1 in matrix  
19 mineralization and bone architecture (Extended Data Fig. 6f). Nevertheless, detailed analysis showed  
20 that the deletion of *Dmp1* in osteoblasts arrested the age-related maturation of the OF. Specifically, type  
21 H vessels together with bulges were preserved in the central part of the OF in *Dmp1*<sup>iΔOB</sup> mice (Fig.  
22 2g,h). Moreover, the difference in EMCN and MMP9 intensity between the central and peripheral parts  
23 of the OF was absent in *Dmp1*<sup>iΔOB</sup> femurs (Fig. 2i,k). The overall EMCN intensity and MMP9 amount  
24 in the OF centre were higher in *Dmp1*<sup>iΔOB</sup> samples compared with the control group (Fig. 2j,l). As  
25 expected, von Kossa staining showed reduced mineralization of the OF in *Dmp1*<sup>iΔOB</sup> femurs, confirming  
26 the crucial importance of DMP1 for bone calcification (Extended Data Fig. 6g,h,j).

27 In line with the phenotype of *Dmp1*<sup>iΔOB</sup> mice at the OF, analysis of subchondral bone revealed that  
28 *Dmp1* deletion at 4 weeks led to preserved density of EMCN<sup>+</sup> vessels and high amounts of MMP9

1 around the vessel tips underneath the articular cartilage by week 6 (Fig. 2m-o). Control mice featured  
2 significantly reduced vessel activity in subchondral bone, whereas *Dmp1*<sup>iΔOB</sup> samples were very similar  
3 to 4-week-old wild-type subchondral bone. Thus, deletion of *Dmp1* at 4 weeks prevented the  
4 development-associated switch from active to quiescent vessel fate not only at the OF but also in  
5 subchondral bone. The mineralization of subchondral bone was also reduced in *Dmp1*<sup>iΔOB</sup> femurs  
6 (Extended Data Fig. 6g,i,k). In summary, these results demonstrate that, apart from its canonical  
7 function in matrix mineralization, DMP1 induces the transformation of active type H into quiescent  
8 type L vessels, which results in reduced EMCN and MMP9 expression and loss of vessel bulges.

9

### 10 **DMP1 inhibits VEGF signalling in the ossification front**

11 To test whether DMP1 has VEGF-inhibiting properties in bone, we studied phosphorylation of the main  
12 VEGF receptor VEGFR2 (pVEGFR2) along with DMP1 accumulation in ECM. Local DMP1 amounts  
13 negatively correlated with the amount of phosphorylated VEGFR2 (Fig. 3a and Extended Data Fig. 7a).  
14 The VEGFR2 phosphorylation level in 4- to 5-week-old mice was equal across the OF. However, at  
15 5.5-6 weeks we observed a marked reduction in the amount of pVEGFR2 in the central part of the OF  
16 in wild-type mice. This difference was largely lost in *Dmp1*<sup>iΔOB</sup> mice, and the overall intensity of  
17 pVEGFR2 in the OF centre was higher (Fig. 3b-d). Of note, the total level of VEGFR2 protein was not  
18 affected by *Dmp1* deletion (Fig. 3e,g).

19 Previous studies showed that VEGFR2 activation induces VEGFR3 expression in endothelial cells<sup>13,14</sup>.  
20 VEGFR3 is usually highly upregulated in endothelial tip cells, where it plays a crucial role in vessel  
21 sprouting<sup>13,15,16</sup>. Bulges in the GP of *Dmp1*<sup>iΔOB</sup> mice stained strongly with VEGFR3 compared with  
22 remaining bulges of control mice (Fig. 3f,h). This result suggests that osteoblast-released DMP1  
23 downregulates VEGFR3 in endothelial tip cells most likely by interference with VEGFR2 signalling,  
24 thus leading to the loss of vessel bulges. Further support came from the finding that treatment of the  
25 capillary endothelial cell line bEnd.3 with DMP1 abrogated the VEGF-induced phosphorylation of  
26 VEGFR2 and the expression of *cfos*, a target gene of VEGF signalling<sup>17</sup> (Extended Data Fig. 7b-d).  
27 Taken together, these data demonstrate that in the OF, DMP1 inhibits VEGF signalling, which is a  
28 known driver of angiogenesis and osteogenesis<sup>18-20</sup>.

1 **Mechanical forces trigger PIEZO1 to enhance FAM20C kinase production and DMP1 secretion**

2 Hormones, especially sex hormones, are usually considered important regulators of bone growth and  
3 metabolism<sup>21-23</sup>. Mice achieve puberty by approximately week 6, which coincides in time with the burst  
4 in DMP1 secretion. We noticed that the extent of DMP1 release at 5.5-6 weeks varied considerably  
5 between individual mice (cf. Fig. 1f). We also noted that in mice with lower body weight than average,  
6 the burst in DMP1 secretion had not yet taken place at 5.5-6 weeks. Inversely, littermates heavier than  
7 average featured already very advanced DMP1 release at this time point (Fig. 3i). Indeed, we found a  
8 positive correlation between body weight and the extent of DMP1 secretion (Fig. 3j). Since DMP1 is  
9 also a key factor in matrix mineralization, we hypothesised that mechanical force, directly or indirectly,  
10 controls DMP1 secretion.

11 FAM20C is the kinase mediating the phosphorylation and subsequent secretion of DMP1 into ECM<sup>4</sup>.  
12 Notably, in 6-week-old mice, we found more FAM20C, along with higher DMP1 accumulation, in the  
13 OF centre in comparison to the periphery, which was not the case in 4-week-old mice (Fig. 3k-m). In  
14 line with FAM20C acting upstream of DMP1, inducible *Dmp1* deletion did not impair FAM20C  
15 upregulation at the age of 6 weeks (Extended Data Fig. 8a,b).

16 To investigate whether FAM20C production was enhanced by mechanical loading, we cultured live  
17 400-500- $\mu$ m-thick slices of 4-week-old femurs and centrifuged them twice daily on 5 consecutive days  
18 (Fig. 4a). Loading via centrifugation caused an upregulation of intracellular FAM20C protein and  
19 enhanced DMP1 secretion (Fig. 4b,c and Extended Data Fig. 8c,d). The mechanically induced FAM20C  
20 upregulation apparently occurred hormone-independently in the cultured femur slices *in vitro*.

21 To study if body weight-associated mechanical forces control FAM20C production also *in vivo*, we  
22 unloaded one hind limb in the mouse by cutting the sciatic and femoral nerves at the age of 4.5 weeks  
23 (Fig. 4d). This results in paralysis of the affected hind limb with all weight going through the  
24 contralateral (normal) side, whereas both limbs were exposed to the same hormonal environment.  
25 Unloading by double neurectomy prevented FAM20C upregulation and DMP1 secretion at 5.5-6 weeks  
26 in almost all of the operated limbs, whilst preserving normal release on the contralateral side (Fig. 4e,f  
27 and Extended Data Fig. 8e,f).

1 In our transcriptome analysis, we found 4 mechanoreceptors that osteoblasts could potentially express  
2 in the OF during late postnatal development: *Trpv4*, *Kcnk2*, *Piezo1*, *Piezo2* (Extended Data Fig. 8g).  
3 Recently published studies show that in osteoblasts, mainly PIEZO1 and to a lesser extent PIEZO2 are  
4 key mechanosensors mediating anabolic effects of loading on bone<sup>24-28</sup>. Thus, we tested whether  
5 PIEZO1 or PIEZO2 control *Fam20c* upregulation in osteoblasts by analysis of bones of 6-7-week-old  
6 mice with *Piezo1* or *Piezo2* deficiency in *Dmp1*-expressing cells (*Piezo1*<sup>Δ*Dmp1*</sup> or *Piezo2*<sup>Δ*Dmp1*</sup>). FAM20C  
7 upregulation and the resulting burst in DMP1 secretion were lost exclusively in *Piezo1*<sup>Δ*Dmp1*</sup> bones but  
8 normal in *Piezo2*<sup>Δ*Dmp1*</sup> femurs (Fig. 4g-m and Extended Data Fig. 8h). Importantly, osteoblast  
9 maturation and abundance were not affected by *Piezo1* deletion both at 4 and 7 weeks (Extended Data  
10 Fig. 8i-k). 4-week-old *Piezo1*<sup>Δ*Dmp1*</sup> bones featured similar levels of FAM20C and DMP1 as control  
11 bones indicating that PIEZO1 mediates the weight-induced upregulation of FAM20C around  
12 periadolescence, whereas basal FAM20C expression is PIEZO1 independent (Extended Data Fig. 8l-  
13 n). To conclude, mechanical forces trigger PIEZO1 to enhance FAM20C expression and subsequent  
14 DMP1 secretion in osteoblasts.

## 15 **Discussion**

16 In this study, we identify a two-step molecular mechanism by which mechanical forces limit growth of  
17 long bones and drive bone maturation at the end of adolescence (Extended Data Fig. 9). First, body  
18 weight-associated mechanical loading triggers the mechanoreceptor PIEZO1 to enhance the production  
19 of FAM20C kinase in osteoblasts, which induces a burst in DMP1 secretion into extracellular matrix.  
20 Second, large amounts of extracellular DMP1 inhibit VEGF signalling in the OF and transform highly-  
21 angiogenic type H vessels into quiescent type L vasculature to arrest bone growth. In parallel,  
22 extracellular DMP1 leads to rapid matrix mineralization and strengthening of long bones<sup>5,29,30</sup>. Thus,  
23 the role of DMP1 in bone is multifaceted: it combines active inhibition of angiogenesis with  
24 mineralizing activity. The discovered link between mechanical loading and FAM20C upregulation, a  
25 major kinase of the bone phosphoproteome, provides a mechanistic explanation for the well-known  
26 positive effect of loading on bone mineralization<sup>31</sup>. Furthermore, it may offer a mechanistic explanation  
27 for hormone-independent osteoporosis caused by lack of loading, for example in astronauts<sup>32,33</sup> or after  
28 long immobilization of a fractured bone<sup>34</sup>.

1 Growth-promoting type H vessels have received much attention in the last years because of their  
2 substantial clinical potential<sup>35,36</sup>. Our finding that inducible *Dmp1* deletion led to increased vessel  
3 activity also in subchondral bone suggests that extracellular DMP1 may protect articular cartilage from  
4 vessel invasion, which accompanies neoinnervation of the tissue and sensation of pain in osteoarthritis  
5 patients<sup>37-38</sup>. Moreover, DMP1-mediated inhibition of angiogenesis in bone may be useful in arresting  
6 growth of tumours including osteo- and chondrosarcomas<sup>39-41</sup>.

7 Under the influence of systemic hormones, bones of male mice acquire higher mass and cortical  
8 thickness than females, which is already evident at early puberty<sup>42</sup> (3-5 weeks). As the weight of male  
9 mice is also greater than females at this stage it is likely that the load perceived by individual osteoblasts  
10 in male and female bones is equivalent during growth according to the principles of isometric scaling<sup>43</sup>.

11 This may explain why the triggering of FAM20C upregulation and DMP1 secretion happens in both  
12 genders at the same age despite the difference in absolute body weight, and presumably after a key  
13 mechanical threshold has been reached. Our results suggest that mechanical force is a key player in the  
14 control of bone growth termination, acting on bones in addition to systemic sex hormones<sup>21-23</sup>.

15 Growth plate injuries are one of the most common types of fractures in children<sup>44</sup> since the OF-GP  
16 border is the weakest and most flexible part of the bone. From an evolutionary perspective, it appears  
17 desirable to have loading-dependent mechanisms as a protective feedback in place that with increasing  
18 body weight, drive bone maturation and improve durability via enhanced calcification and simultaneous  
19 growth inhibition.

20 Based on our finding that FAM20C upregulation is induced by loading and it happens first in the OF  
21 centre, we hypothesize that the central part of the OF is exposed to the highest mechanical strain since  
22 it is a spot where the loading from all four domes of the GP gets integrated. Moreover, there is no  
23 cortical bone underneath to absorb this loading (Extended Data Fig. 8o).

24 The findings presented here demonstrate that mechanical forces transmitted through PIEZO1 play a  
25 crucial role in the regulation of skeletal development and bone maturation via FAM20C-mediated  
26 extracellular DMP1 accumulation and its control of blood vessel subtypes in bone. This knowledge may  
27 be applied in bone healing studies<sup>45</sup>, as well as in different kinds of bone pathologies featuring abnormal  
28 bone growth activity, including osteoarthritis, osteosarcoma and osteoporosis.

## 1 **Acknowledgments**

2 We thank Prof. Dr. T. Blankenstein for providing *Coll-CreERT2* mice; Prof. Dr. A. Hamann for  
3 providing bEnd.3 cell line; Dr. G. Heinz and K. Lehmann for help with cDNA library preparation; V.  
4 Holecska and C. Ruster for technical assistance; M. Drabkina for advice on RNAScope technique; and  
5 Dr. P. Saikali, V. Plajer and Dr. C. Helmstetter for advice and consultation. **Funding:** This work was  
6 supported by the Willy Robert Pitzer Foundation (Osteoarthritis Research Program), the state of Berlin  
7 and the European Regional Development Fund (ERDF 2014–2020, EFRE 1.8/11), Deutsche  
8 Forschungsgemeinschaft (grant no. AM 103/31-1), Centre for OA Pathogenesis Versus Arthritis (grant  
9 no. 21621). M.D. and T.M.B. were fellows of the International Max Planck Research School for  
10 Infectious Diseases and Immunology.

## 11 **Author Contributions**

12 M.D. and M.L. designed the experiments, interpreted the results and wrote the manuscript. T.M.B.  
13 helped with the generation of the transgenic mouse lines and *in vivo* experiments and provided technical  
14 expertise. J.M.Z. performed and T.L.V. supervised double neurectomy experiments. F.H. and M.F.M.  
15 provided transcriptome analysis. L.B. and T.S. provided *Piezo1<sup>ΔDmp1</sup>* and *Piezo2<sup>ΔDmp1</sup>* samples. A.K.,  
16 T.S. and T.L.V. provided expertise and advice. R.K. designed and generated *Dmp1<sup>-/-</sup>* and *Dmp1<sup>fl/fl</sup>* mice.  
17 M.D. performed all other experiments and analysed the data. All authors reviewed and edited the  
18 manuscript.

## 19 **Declaration of Interests**

20 The authors declare no competing interests.

## 21 **Data and Materials Availability**

22 RNA sequencing data are available at gene expression omnibus (GEO) under the accession number  
23 GSE148804. All other data supporting the findings of this study are available from the corresponding  
24 author on request.

25

## 1 References

- 2 1. Kusumbe, A. P., Ramasamy, S. K. & Adams, R. H. Coupling of angiogenesis and  
3 osteogenesis by a specific vessel subtype in bone. *Nature* **507**, 323–328 (2014).
- 4 2. Ramasamy, S. K., Kusumbe, A. P., Wang, L. & Adams, R. H. Endothelial Notch activity  
5 promotes angiogenesis and osteogenesis in bone. *Nature* **507**, 376–380 (2014).
- 6 3. Romeo, S. G. *et al.* Endothelial proteolytic activity and interaction with non-resorbing  
7 osteoclasts mediate bone elongation. *Nature Cell Biology* **21**, 430–441 (2019).
- 8 4. Liu, P. *et al.* Specific ablation of mouse Fam20C in cells expressing type I collagen leads to  
9 skeletal defects and hypophosphatemia. *Scientific Reports* **7**, 3590 (2017).
- 10 5. Feng, J. Q. *et al.* Loss of DMP1 causes rickets and osteomalacia and identifies a role for  
11 osteocytes in mineral metabolism. *Nature Genetics* **38**, 1310–1315 (2006).
- 12 6. Pirotte, S. *et al.* Dentin matrix protein 1 induces membrane expression of VE-cadherin on  
13 endothelial cells and inhibits VEGF-induced angiogenesis by blocking VEGFR-2  
14 phosphorylation. *Blood* **117**, 2515–2526 (2011).
- 15 7. Feng, J. Q. *et al.* The dentin matrix protein 1 (Dmp1) is specifically expressed in mineralized,  
16 but not soft, tissues during development. *Journal of Dental Research* **82**, 776–780 (2003).
- 17 8. Delgado-Calle, J., Sato, A. Y. & Bellido, T. Role and mechanism of action of sclerostin in  
18 bone. *Bone* **96**, 29–37 (2017).
- 19 9. Romeo, S. G. *et al.* Endothelial proteolytic activity and interaction with non-resorbing  
20 osteoclasts mediate bone elongation. *Nature Cell Biology* **21**, 430–441 (2019).
- 21 10. Ye, L. *et al.* Dmp1-deficient mice display severe defects in cartilage formation responsible for  
22 a chondrodysplasia-like phenotype. *Journal of Biological Chemistry* **280**, 6197–6203 (2005).
- 23 11. Lorenz-Depiereux, B. *et al.* DMP1 mutations in autosomal recessive hypophosphatemia  
24 implicate a bone matrix protein in the regulation of phosphate homeostasis. *Nature Genetics*  
25 **38**, 1248–1250 (2006).
- 26 12. Rios, H. F. *et al.* DMP1 is essential for osteocyte formation and function. *Journal of*  
27 *Musculoskeletal Neuronal Interactions* **5**, 325–327 (2005).
- 28 13. Tammela, T. *et al.* Blocking VEGFR-3 suppresses angiogenic sprouting and vascular network  
29 formation. *Nature* **454**, 656–660 (2008).
- 30 14. Zarkada, G., Heinolainen, K., Makinen, T., Kubota, Y. & Alitalo, K. VEGFR3 does not  
31 sustain retinal angiogenesis without VEGFR2. *Proceedings of the National Academy of*  
32 *Sciences of the United States of America* **112**, 761–766 (2015).
- 33 15. Tammela, T. *et al.* VEGFR-3 controls tip to stalk conversion at vessel fusion sites by  
34 reinforcing Notch signalling. *Nature Cell Biology* **13**, 1202–1213 (2011).
- 35 16. Langen, U. H. *et al.* Cell-matrix signals specify bone endothelial cells during developmental  
36 osteogenesis. *Nature Cell Biology* **19**, 189–201 (2017).
- 37 17. Holmes, D. I. R. & Zachary, I. Placental growth factor induces FosB and c-Fos gene  
38 expression via Flt-1 receptors. *FEBS Letters* **557**, 93–98 (2004).
- 39 18. Olsson, A. K., Dimberg, A., Kreuger, J. & Claesson-Welsh, L. VEGF receptor signalling - In  
40 control of vascular function. *Nature Reviews Molecular Cell Biology* **7**, 359–371 (2006).
- 41 19. Wang, S. *et al.* Control of endothelial cell proliferation and migration by VEGF signalling to  
42 histone deacetylase 7. *Proceedings of the National Academy of Sciences of the United States of*  
43 *America* **105**, 7738–7743 (2008).
- 44 20. Yang, Y. Q. *et al.* The role of vascular endothelial growth factor in ossification. *International*  
45 *Journal of Oral Science* **4**, 64–68 (2012).
- 46 21. Nilsson, O., Marino, R., de Luca, F., Phillip, M. & Baron, J. Endocrine regulation of the  
47 growth plate. *Hormone Research* **64**, 157–165 (2005).
- 48 22. Khosla, S. & Monroe, D. G. Regulation of bone metabolism by sex steroids. *Cold Spring*  
49 *Harbor Perspectives in Medicine* **8**, a031211 (2018).
- 50 23. Chagin, A. S. *et al.* Estrogen receptor- $\beta$  inhibits skeletal growth and has the capacity to  
51 mediate growth plate fusion in female mice. *Journal of Bone and Mineral Research* **19**, 72–77  
52 (2004).
- 53 24. Li, X. *et al.* Stimulation of Piezo1 by mechanical signals promotes bone anabolism. *eLife* **8**,  
54 e49631 (2019).

- 1 25. Sun, W. *et al.* The mechanosensitive Piezo1 channel is required for bone formation. *eLife* **8**,  
2 e47454 (2019).
- 3 26. Zhou, T. *et al.* Piezo1/2 mediate mechanotransduction essential for bone formation through  
4 concerted activation of NFAT-YAP1- $\beta$ -catenin. *eLife* **9**, e52779 (2020).
- 5 27. Wang, L. *et al.* Mechanical sensing protein PIEZO1 regulates bone homeostasis via  
6 osteoblast-osteoclast crosstalk. *Nature Communications* **11**, 282 (2020).
- 7 28. Hendrickx, G. *et al.* Piezo1 Inactivation in Chondrocytes Impairs Trabecular Bone  
8 Formation. *Journal of Bone and Mineral Research*, jbmr.4198 (2020).
- 9 29. He, G. & George, A. Dentin Matrix Protein 1 Immobilized on Type I Collagen Fibrils  
10 Facilitates Apatite Deposition in Vitro. *Journal of Biological Chemistry* **279**, 11649–11656  
11 (2004).
- 12 30. Ling, Y. *et al.* DMP1 depletion decreases bone mineralization in vivo: An FTIR imaging  
13 analysis. *Journal of Bone and Mineral Research* **20**, 2169–2177 (2005).
- 14 31. Ozcivici, E. *et al.* Mechanical signals as anabolic agents in bone. *Nature Reviews*  
15 *Rheumatology* **6**, 50–59 (2010).
- 16 32. Lang, T. *et al.* Cortical and trabecular bone mineral loss from the spine and hip in long-  
17 duration spaceflight. *Journal of Bone and Mineral Research* **19**, 1006–1012 (2004).
- 18 33. Keyak, J. H., Koyama, A. K., LeBlanc, A., Lu, Y. & Lang, T. F. Reduction in proximal  
19 femoral strength due to long-duration spaceflight. *Bone* **44**, 449–453 (2009).
- 20 34. Ceroni, D. *et al.* Effects of cast-mediated immobilization on bone mineral mass at various  
21 sites in adolescents with lower-extremity fracture. *Journal of Bone and Joint Surgery - Series*  
22 *A* **94**, 208–216 (2012).
- 23 35. Peng, Y., Wu, S., Li, Y. & Crane, J. L. Type H blood vessels in bone modeling and  
24 remodeling. *Theranostics* **10**, 426–436 (2020).
- 25 36. Xu, R. *et al.* Targeting skeletal endothelium to ameliorate bone loss. *Nature Medicine* **24**,  
26 823–833 (2018).
- 27 37. Suri, S. *et al.* Neurovascular invasion at the osteochondral junction and in osteophytes in  
28 osteoarthritis. *Annals of the Rheumatic Diseases* **66**, 1423–1428 (2007).
- 29 38. Vincent, T. L. Peripheral pain mechanisms in osteoarthritis. *Pain* **161**, S138–S146 (2020).
- 30 39. Duffaud, F. *et al.* Efficacy and safety of regorafenib in adult patients with metastatic  
31 osteosarcoma: a non-comparative, randomised, double-blind, placebo-controlled, phase 2  
32 study. *The Lancet Oncology* **20**, 120–133 (2019).
- 33 40. Davis, L. E. *et al.* Randomized double-blind phase II study of regorafenib in patients with  
34 metastatic osteosarcoma. *Journal of Clinical Oncology* **37**, 1424–1431 (2019).
- 35 41. Chow, W. *et al.* Results of a prospective phase 2 study of pazopanib in patients with  
36 surgically unresectable or metastatic chondrosarcoma. *Cancer* **126**, 105–111 (2020).
- 37 42. Callewaert, F. *et al.* Sexual dimorphism in cortical bone size and strength but not density is  
38 determined by independent and time-specific actions of sex steroids and IGF-1: Evidence from  
39 pubertal mouse models. *Journal of Bone and Mineral Research* **25**, 617–626 (2010).
- 40 43. Stern, T. *et al.* Isometric scaling in developing long bones is achieved by an optimal  
41 epiphyseal growth balance. *PLoS Biology* **13**, e1002212 (2015).
- 42 44. Jones, C., Wolf, M. & Herman, M. Acute and chronic growth plate injuries. *Pediatrics in*  
43 *Review* **38**, 129–138 (2017).
- 44 45. McDermott, A. M. *et al.* Recapitulating bone development through engineered mesenchymal  
45 condensations and mechanical cues for tissue regeneration. *Science Translational Medicine*  
46 **11**, eaav7756 (2019).
- 47

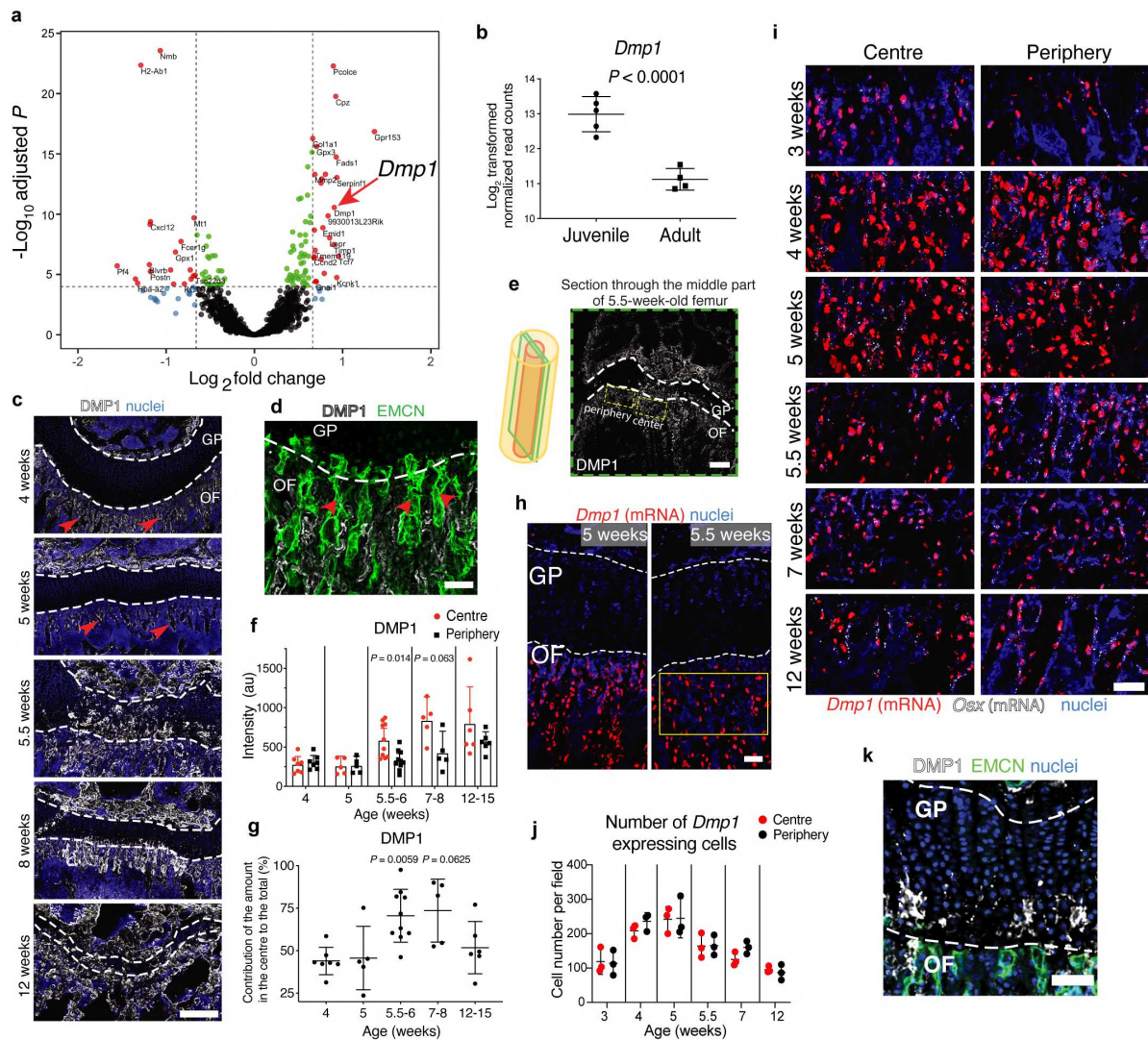


**Fig. 1: Burst in DMP1 secretion from osteoblasts into ECM at the OF-GP border during periadolescence.**  
**a**, Volcano plot of significantly differentially expressed genes in juvenile (4 weeks, n=5) versus adult (12 weeks, n=4) capillary with surrounding cells from the ossification front (OF) (mean expression value >500, red:  $\text{Log}_2 \text{FC} > 0.66$ ,  $P < 10^{-5}$ ). **b**,  $\text{Log}_2$  transformed number of reads mapped to the *Dmp1* gene. **c**, DMP1 immunostaining in the OF throughout postnatal bone development. Red arrows point at DMP1 at the OF base. Scale bar 250  $\mu\text{m}$ . **d**, DMP1 and endomucin (EMCN) immunostaining of the OF from 5-week-old femur. Red arrows point at type H vessels. Scale bar 50  $\mu\text{m}$ . **e**, Schematic depiction of the femur with a green plane going through the centre of the bone, where DMP1 secretion is observed. Example of DMP1 immunostaining of a section taken from the middle part of the femur, showing the definition of the central and peripheral regions used for further automated quantification. Scale bar 250  $\mu\text{m}$ . **f**, Quantification of DMP1 staining intensity in the centre and periphery of the OF throughout bone development. Mean  $\pm$  SD. **g**, Quantification of the contribution of the central and peripheral part to the total DMP1 amount. Mean  $\pm$  SD. **f,g**, at 4 weeks n=7, 5 weeks n=5, 5.5-6 weeks n=10, 8 weeks n=5, 12-15 weeks n=6. Pooled data from 5 independent experiments. *P* values show the significance between the intensity in the centre versus periphery for every mouse (paired analysis). Two-tailed Wilcoxon matched-pairs signed rank test. **h**, *Dmp1* mRNA (RNAScope) of the central regions of OF and GP from 5- and 5.5-week-old femurs. Lack of *Dmp1* expression in chondrocytes of the GP; yellow frame indicates the region shown in Fig. 1i. Scale bar 50  $\mu\text{m}$ . **i**, RNAScope images of *Dmp1*, Osterix (*Osx*) and *Runx2* (only depicted in Extended Data Fig. 2c). Scale bar 50  $\mu\text{m}$ . **j**, Number of *Dmp1*-expressing cells in the central and peripheral region of the OF based on RNAScope images. n=3 per age. Pooled data from 2 independent experiments. Mean  $\pm$  SD. **k**, DMP1 and EMCN immunostaining of 5.5-week-old femur. Infiltration of DMP1 from the OF into the GP. Scale bar 50  $\mu\text{m}$ .

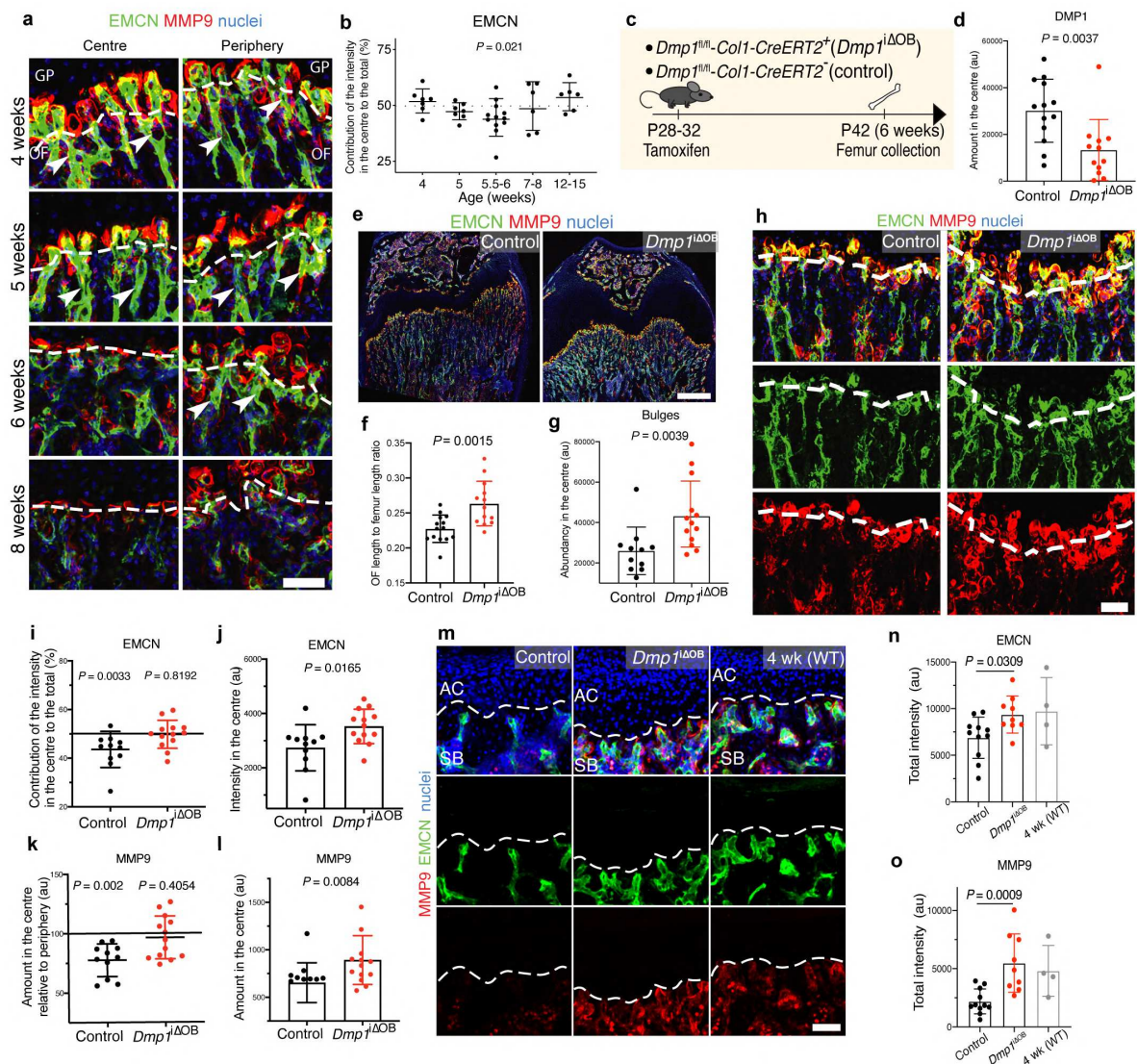


**Fig. 2: DMP1 transforms active type H vessels into quiescent type L in the ossification front and in subchondral bone.**  
**a.** EMCN and MMP9 immunostaining of femur throughout postnatal development. Dashed line shows the OF-GP border. White arrows point at type H vessels. Scale bar 50  $\mu$ m. **b.** Quantification of the contribution of the central and peripheral parts to the total EMCN intensity. At 4 and 5 weeks n=7, 5.5-6 weeks n=12, 8 weeks n=6, 12-15 weeks n=6. Pooled data from 6 independent experiments.  $P$  value shows the significance between the intensity in the centre versus periphery for every mouse (two-tailed paired  $t$ -test, significant only for 5.5-6 weeks). Mean  $\pm$  SD. **c.** Experimental scheme to induce  $Dmp1$  deletion by Tamoxifen injection starting at 4 weeks (P28-32) and to analyse bones at 6 weeks (P42). **d.** Quantification of DMP1 protein amount in the OF centre of control and osteoblast-specific inducible  $Dmp1$ -deleted ( $Dmp1^{\Delta OB}$ ) mice. Two-tailed Mann Whitney test. **e.** EMCN and MMP9 immunostaining of 6-week-old control and  $Dmp1^{\Delta OB}$  femurs. Scale bar 500  $\mu$ m. **f.** Quantification of ossification front length to femur length ratio in control and  $Dmp1^{\Delta OB}$  mice. **d,f.** Control n=14,  $Dmp1^{\Delta OB}$  n=13. **g.** Quantification of bulges by measuring the total EMCN intensity in the central bottom part of the GP (500 $\mu$ m long) in control and  $Dmp1^{\Delta OB}$  mice. Two-tailed Mann Whitney test. **h.** EMCN and MMP9 immunostaining of femur in 6-week-old control and  $Dmp1^{\Delta OB}$  mice. Dashed line shows the OF-GP border. Scale bar 50  $\mu$ m. **i.** Quantification of the central to peripheral intensity ratio of EMCN in control and  $Dmp1^{\Delta OB}$  OF. Two-tailed paired  $t$ -test. **j.** Quantification of the total central EMCN intensity in control and  $Dmp1^{\Delta OB}$  group. Two-tailed unpaired  $t$ -test. **k.** Quantification of MMP9 in the centre relative to the periphery at the OF-GP border in control and  $Dmp1^{\Delta OB}$  femurs. Two-tailed paired  $t$ -test. **l.** Quantification of the total central MMP9 amount at the OF-GP border in control and  $Dmp1^{\Delta OB}$  group. Two-tailed Mann Whitney test. **g-l.** Pooled data from 3 independent experiments. Control n=11,  $Dmp1^{\Delta OB}$  n=13. Age: 6 weeks. Mean  $\pm$  SD. **m.** EMCN and MMP9 immunostaining of 6-week-old control,  $Dmp1^{\Delta OB}$  and 4-week-old wild-type (WT) subchondral bone (SB) with articular cartilage (AC). Dashed line indicates the SB-AC border. Scale bar 50  $\mu$ m. **n.** Quantification of the total EMCN intensity at the SB-AC border (500  $\mu$ m long). **o.** Quantification of the total MMP9 intensity around the vessels at the SB-AC border (500  $\mu$ m long). **m-o.** Pooled data from 2 independent experiments. Control n=11,  $Dmp1^{\Delta OB}$  n=9, 4-week-old WT n=4. Mean  $\pm$  SD.

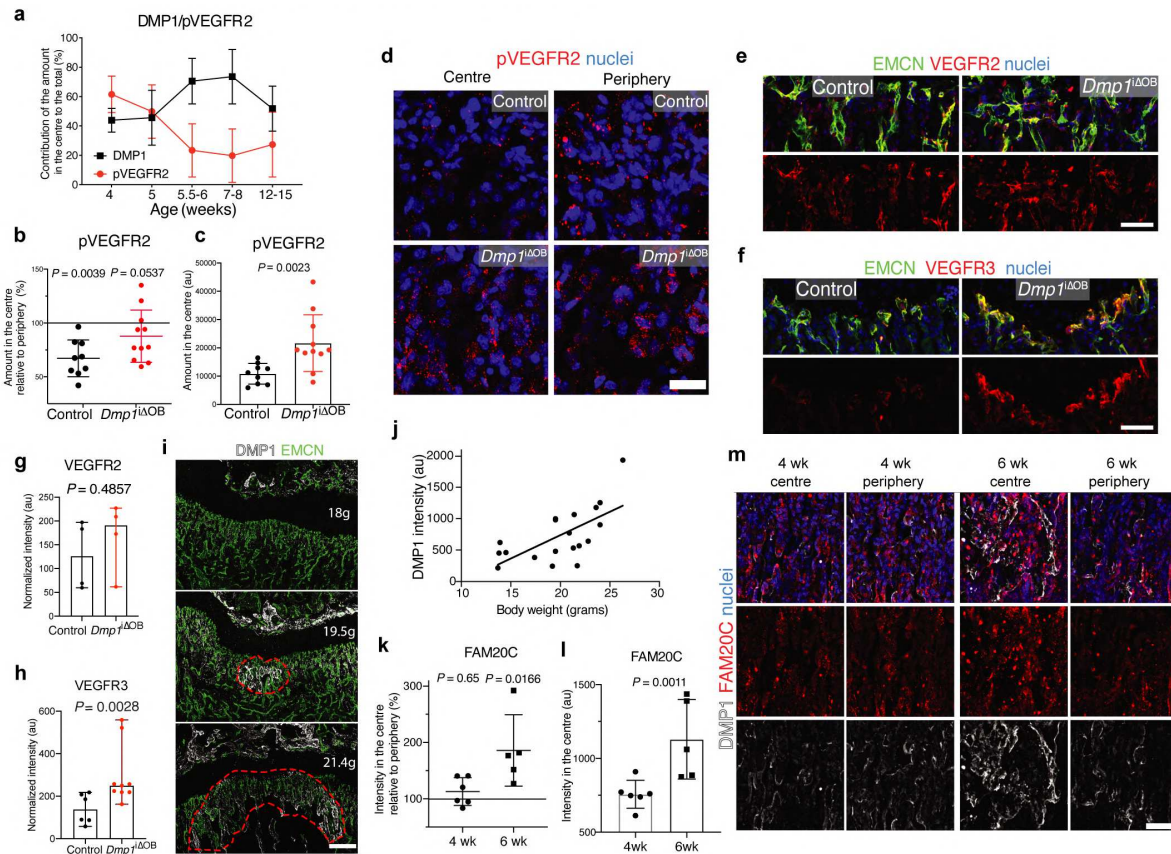


**Fig. 3: Extracellular DMP1 inhibits VEGF signalling in the OF and coincides spatiotemporally with FAM20C upregulation.** **a**, Quantification of the centre to periphery ratio of phosphorylated VEGFR2 (pVEGFR2) and DMP1 amount at different ages. At 4 and 5 weeks n=7, 5.5-6 weeks n=6, 8 weeks n=5, 12-15 weeks n=4. Pooled data from 3 independent experiments. Mean  $\pm$  SD. **b**, Quantification of pVEGFR2 amount in the centre relative to periphery in control and *Dmp1* $\Delta$ OB OF. Two-tailed Wilcoxon matched-pairs signed rank test. **c**, Quantification of the total central pVEGFR2 amount in control and *Dmp1* $\Delta$ OB group. Two-tailed unpaired *t*-test. **b,c**, Pooled data from 3 independent experiments. Control n=9, *Dmp1* $\Delta$ OB n=11. Age: 6 weeks. Mean  $\pm$  SD. **d**, pVEGFR2 immunostaining showing no decrease of pVEGFR2 in the OF centre of *Dmp1* $\Delta$ OB femurs in contrast to control femurs at 6 weeks of age. Scale bar 25  $\mu$ m. **e,f**, VEGFR2 and EMCN (**e**) and VEGFR3 and EMCN (**f**) immunostaining of the OF centre in 6-week-old control and *Dmp1* $\Delta$ OB mice. Scale bar 50  $\mu$ m. **g**, Quantification of VEGFR2 intensity in EMCN<sup>+</sup> endothelial cells in the OF of control and *Dmp1* $\Delta$ OB mice. Control n=4, *Dmp1* $\Delta$ OB n=4. Pooled data from 2 independent experiments. Two-tailed Mann Whitney test. Median  $\pm$  range. **h**, Quantification of VEGFR3 intensity in the OF of control and *Dmp1* $\Delta$ OB mice. Control n=6, *Dmp1* $\Delta$ OB n=9. Pooled data from 3 independent experiments. Two-tailed Mann Whitney test. Median  $\pm$  range. **i**, DMP1 and EMCN immunostaining of 5.5-week-old femurs derived from littermate mice. Red dotted line marks the area of extracellular DMP1 at the OF. Scale bar 250  $\mu$ m. **j**, Counterplot of body weight versus DMP1 intensity.  $R^2 = 0.4139$ , n=19. **k**, Quantification of FAM20C intensity in the centre relative to periphery (centre + periphery) in 4- and 6-week-old femurs. Two-tailed paired *t*-test. **l**, Quantification of FAM20C intensity in the centre in 4- and 6-week-old femurs. Two-tailed paired *t*-test. **k,l**, Pooled data from 2 independent experiments. At 4 weeks n=6, 6 weeks n=5. **m**, FAM20C and DMP1 immunostaining in OF of 4- and 6-week-old femurs. Scale bar 50  $\mu$ m.

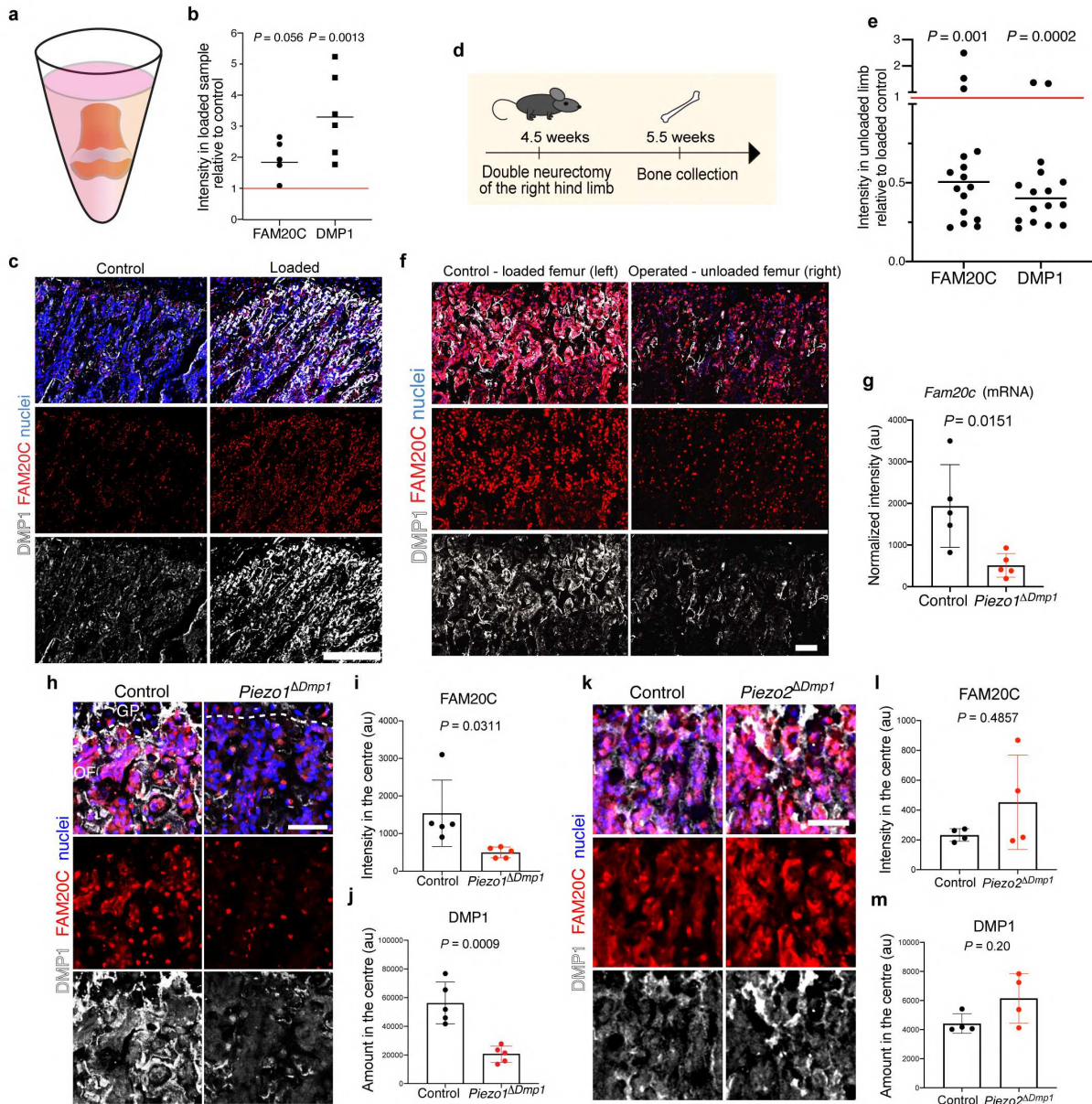
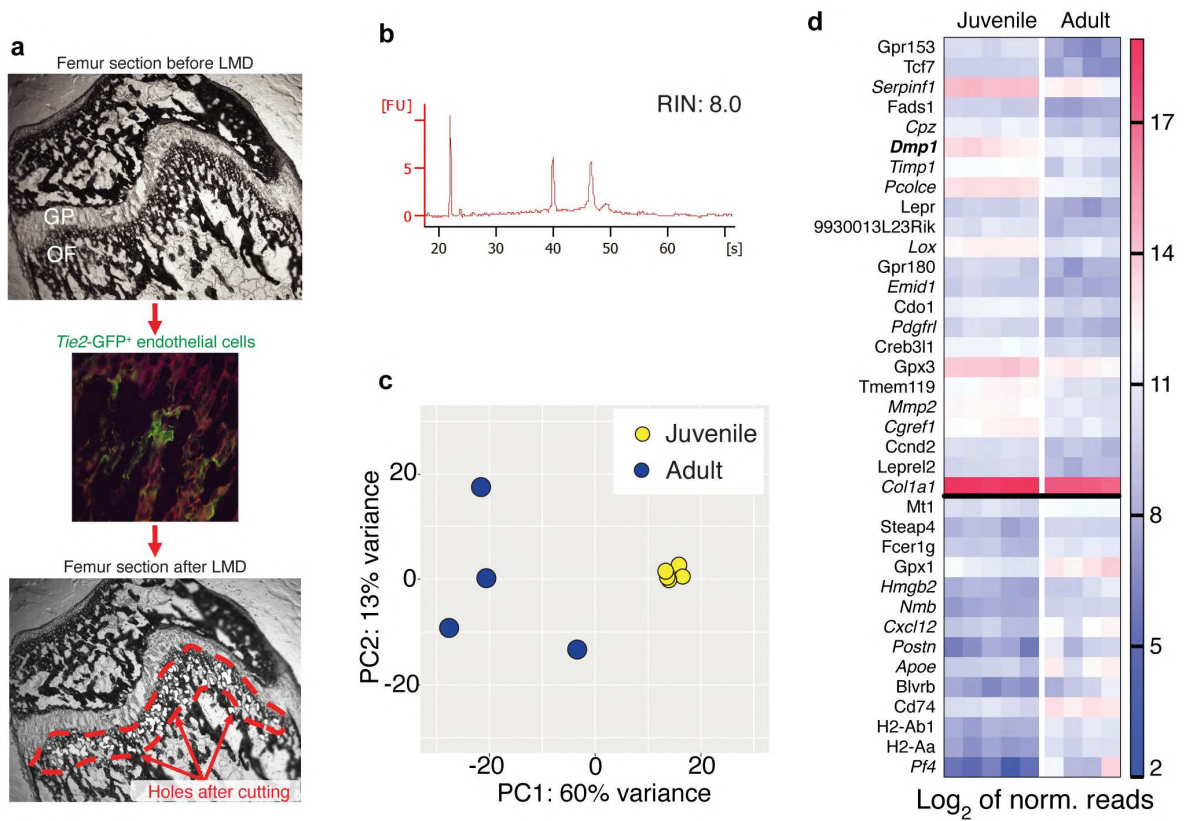


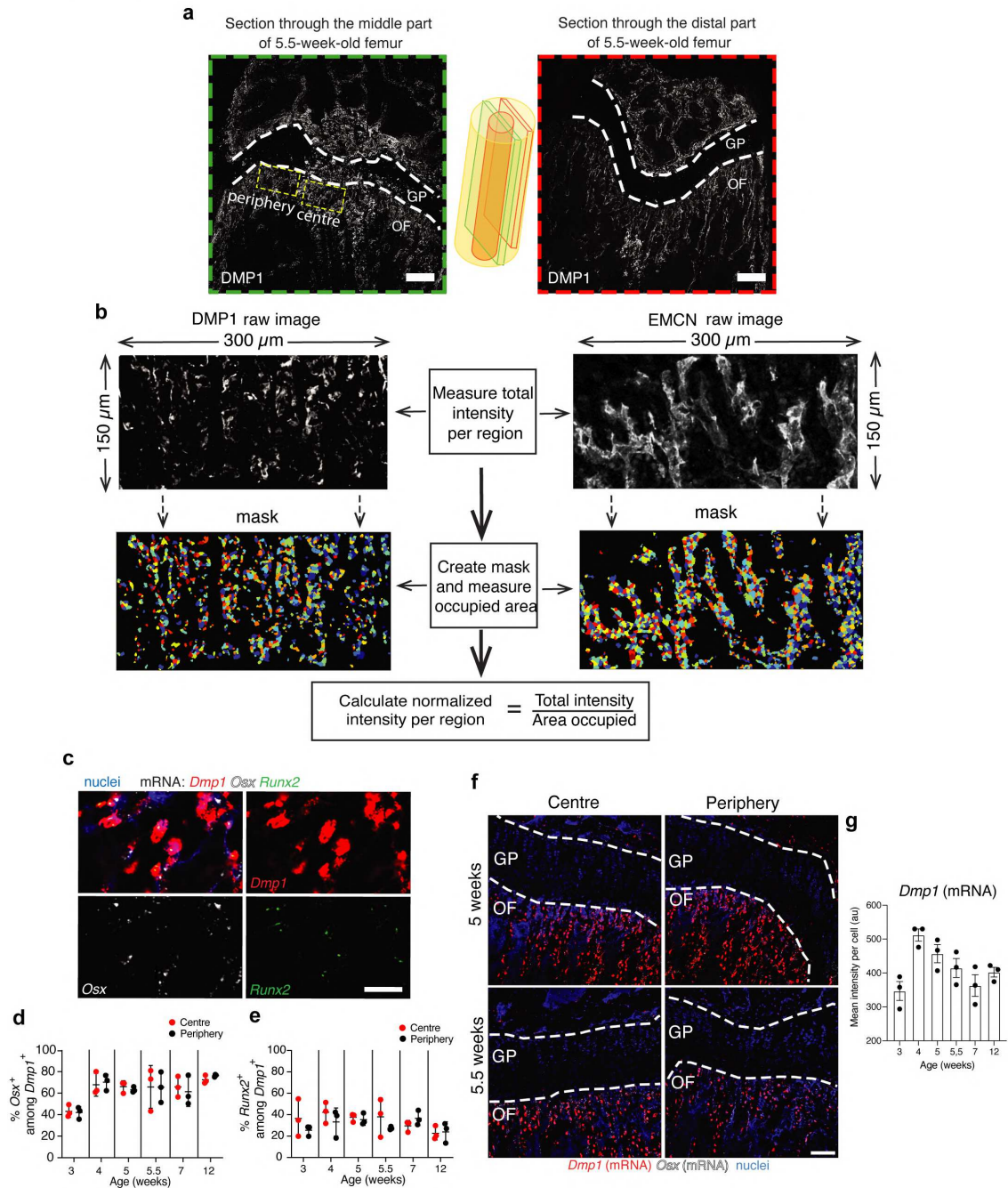
**Fig. 4: Mechanical forces trigger PIEZO1 to enhance FAM20C kinase production and DMP1 secretion.**

**a**, Schematic depiction of the position of a femur slice ( $\approx 500 \mu\text{m}$  thick) derived from 4-week-old mice in a well of a 96-well PCR plate filled with cell culture medium. The slices were either just cultured for 5 days (control) or exposed to loading via low-speed centrifugation (30 min. at 19g) twice per day (loaded). **b**, Quantification of FAM20C and DMP1 intensities in the loaded (centrifuged) samples relative to control (non-centrifuged) group (red line). Pooled data from 2 independent experiments. Mean,  $n=5-6$ .  $P$  values for paired analysis of samples derived from one mouse. Two-tailed paired  $t$ -test. **c**, FAM20C and DMP1 immunostaining of control and loaded (centrifuged) femur slices. Scale bar 100  $\mu\text{m}$ . **d**, Experimental setup for hind limb unloading via sciatic and femoral double neurectomy at the age of 4.5 weeks. **e**, Quantification of FAM20C and DMP1 intensities in the unloaded femur relative to the loaded control (red line) at 5.5 weeks.  $P$  values show significance after paired analysis of intensities derived from the same mouse. Pooled data from 2 independent experiments. Two-tailed Wilcoxon matched-pairs signed rank test. Median,  $n=16$ . **f**, FAM20C and DMP1 immunostaining of loaded (control, left hind limb) and unloaded (operated, right hind limb) femurs at 5.5 weeks. Scale bar 50  $\mu\text{m}$ . **g**, Quantification of *Fam20c* mRNA based on RNAScope images of 7-week-old control and *Piezo1* $\Delta\text{Dmp1}$  OF.  $n=5$ . Two-tailed unpaired  $t$ -test. **h**, FAM20C and DMP1 immunostaining of 7-week-old control and *Piezo1* $\Delta\text{Dmp1}$  OF. Scale bar 50  $\mu\text{m}$ . **i, j**, Quantification of FAM20C (**i**) and DMP1 (**j**) intensities in 7-week-old control and *Piezo1* $\Delta\text{Dmp1}$  OF.  $n=5$ . Two-tailed unpaired  $t$ -test. **k**, FAM20C and DMP1 immunostaining of 6-week-old control and *Piezo2* $\Delta\text{Dmp1}$  OF. Scale bar 50  $\mu\text{m}$ . **l, m**, Quantification of FAM20C (**l**) and DMP1 (**m**) intensities in 6-week-old control and *Piezo2* $\Delta\text{Dmp1}$  OF.  $n=4$ . Two-tailed unpaired  $t$ -test.

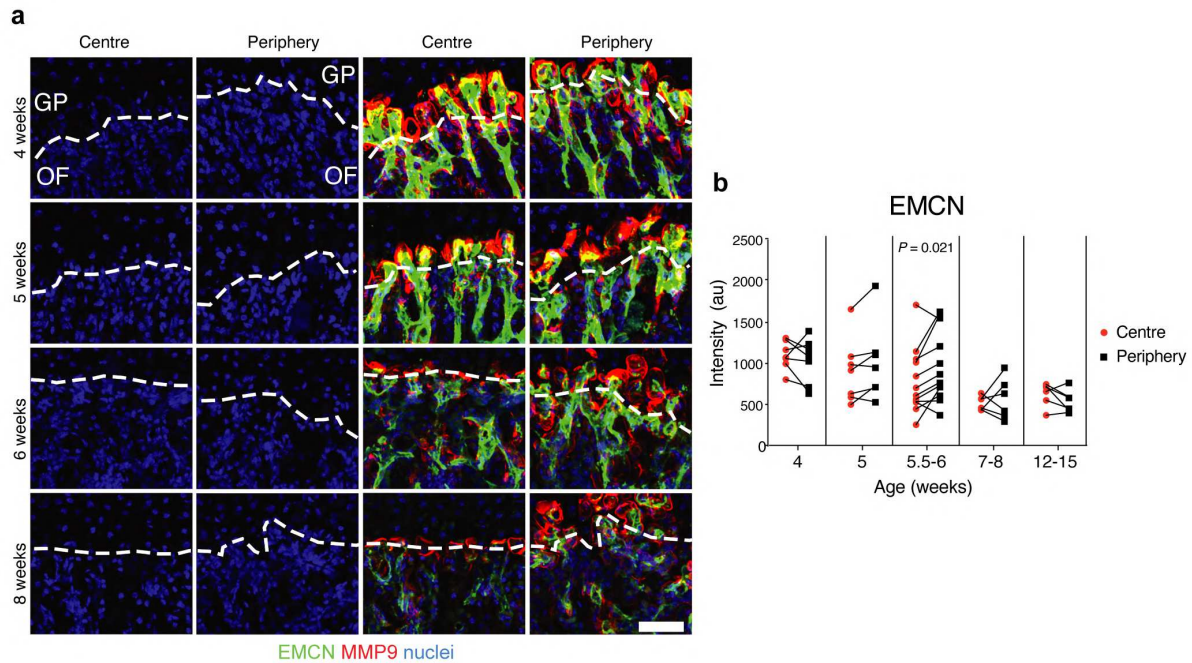
1 Extended Data



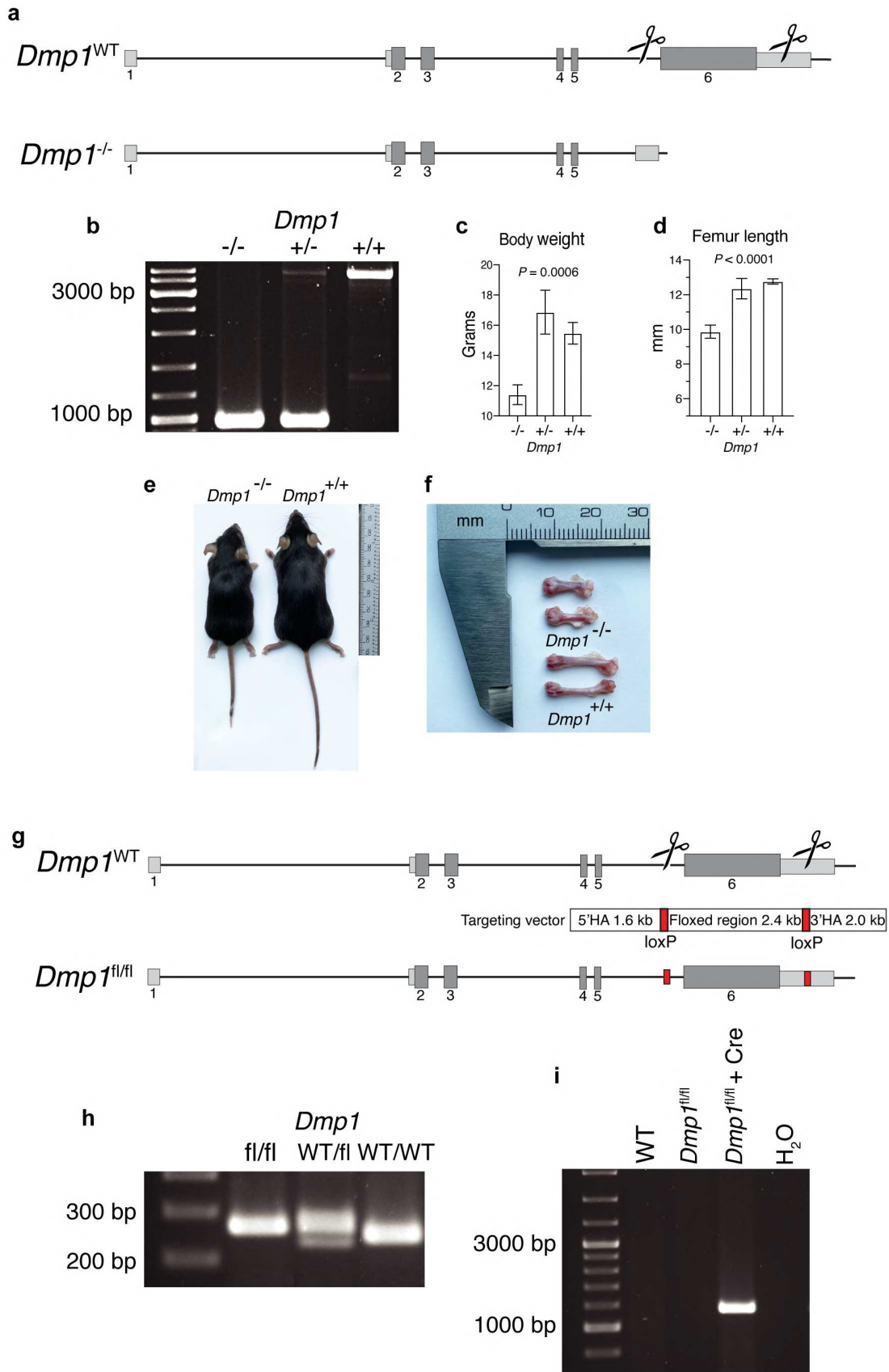
2 **Extended Data Fig. 1: Laser microdissection and sequencing of endothelial cells with surrounding cells**  
 3 **from ossification front of juvenile and adult femurs. a**, Image of the metaphysis in a section from a snap-frozen  
 4 femur directly before laser microdissection (LMD) (top). Epifluorescent image of Tie2-GFP<sup>+</sup> endothelial cells in the  
 5 OF of the snap-frozen femur (middle). GFP<sup>+</sup> regions were cut out and collected. Image of the metaphysis directly  
 6 after LMD with visible holes after cutting out the capillary with surrounding cells, which were collected for further  
 7 transcriptome analysis via next-generation sequencing (NGS) (bottom). **b**, Bioanalyzer plot showing good RNA  
 8 integrity number (RIN) of RNA isolated from laser-microdissected sample from femur section processed according  
 9 to the protocol we developed. The sample consisted of larger laser-microdissected pieces from OF, since the  
 10 amount of RNA in the real sample (single capillary with surrounding cells) was below the detection limit of  
 11 Bioanalyzer. **c**, Principal component analysis of the juvenile (4-week-old) and adult (12-week-old) capillary with  
 12 surrounding cells from OF, which we obtained via LMD, showing that most of the difference is derived from the  
 13 different sample groups and the heterogeneity within the group increases with ageing. **d**, Heat map of the most  
 14 highly and significantly differentially regulated genes in the juvenile versus adult group, where dentin matrix protein  
 15 1 (*Dmp1*) was identified as an interesting candidate for further analysis. Genes encoding ECM proteins are set in  
 16 *italics*. Mean expression value >500, Log<sub>2</sub> FC > 0.66, *P* < 10<sup>-5</sup>.  
 17



1 **Extended Data Fig. 2: Osteoblasts are the main DMP1 producer in the metaphysis and automated**  
 2 **quantification strategy of histological images. a**, DMP1 immunostaining of sections taken from the middle (left  
 3 image, green plane in the scheme) or distal (right image, red plane in the scheme) part of the femur. Yellow dashed  
 4 rectangles indicate the analysis areas that were defined as centre and periphery and used for further automated  
 5 quantification. **b**, Scheme explaining the automated quantification strategy of images using CellProfiler software.  
 6 First, the total intensity of the raw image, which is always the same size ( $4.5 \times 10^4 \mu\text{m}^2$ ), was measured and then  
 7 the area occupied by the protein was calculated by creating a mask. Then the normalized intensity was calculated  
 8 by dividing the total intensity by the occupied area (DMP1, EMCN) or by the total cell density (FAM20C). When the  
 9 total amount of a protein per region was analysed, we used the total intensity without further normalization to the  
 10 area occupied by it (DMP1, pVEGFR2, MMP9). **c**, *Dmp1*, *Osx* and *Runx2* RNAScope staining in the OF of a 5-  
 11 week-old femur. Scale bar 20 μm. **d,e**, Quantification of **(d)** *Osx*<sup>+</sup> and **(e)** *Runx2*<sup>+</sup> cells among *Dmp1*-expressing  
 12 cells based on RNAScope images. n=3 per age. Pooled data from 2 independent experiments. Mean ± SD. **f**,  
 13 *Dmp1* and *Osx* RNAScope overview images from central and peripheral parts of the metaphysis at 5 and 5.5 weeks  
 14 demonstrating the absence of *Dmp1* expression in the GP. **g**, Quantification of the mean *Dmp1* intensity per cell  
 15 among *Dmp1*-expressing cells showing the peak at 4 weeks. n=3 per age,  $4 \times 10^5 \mu\text{m}^2$  area was always analysed  
 16 per sample. Pooled data from 2 independent experiments. Mean ± SEM.

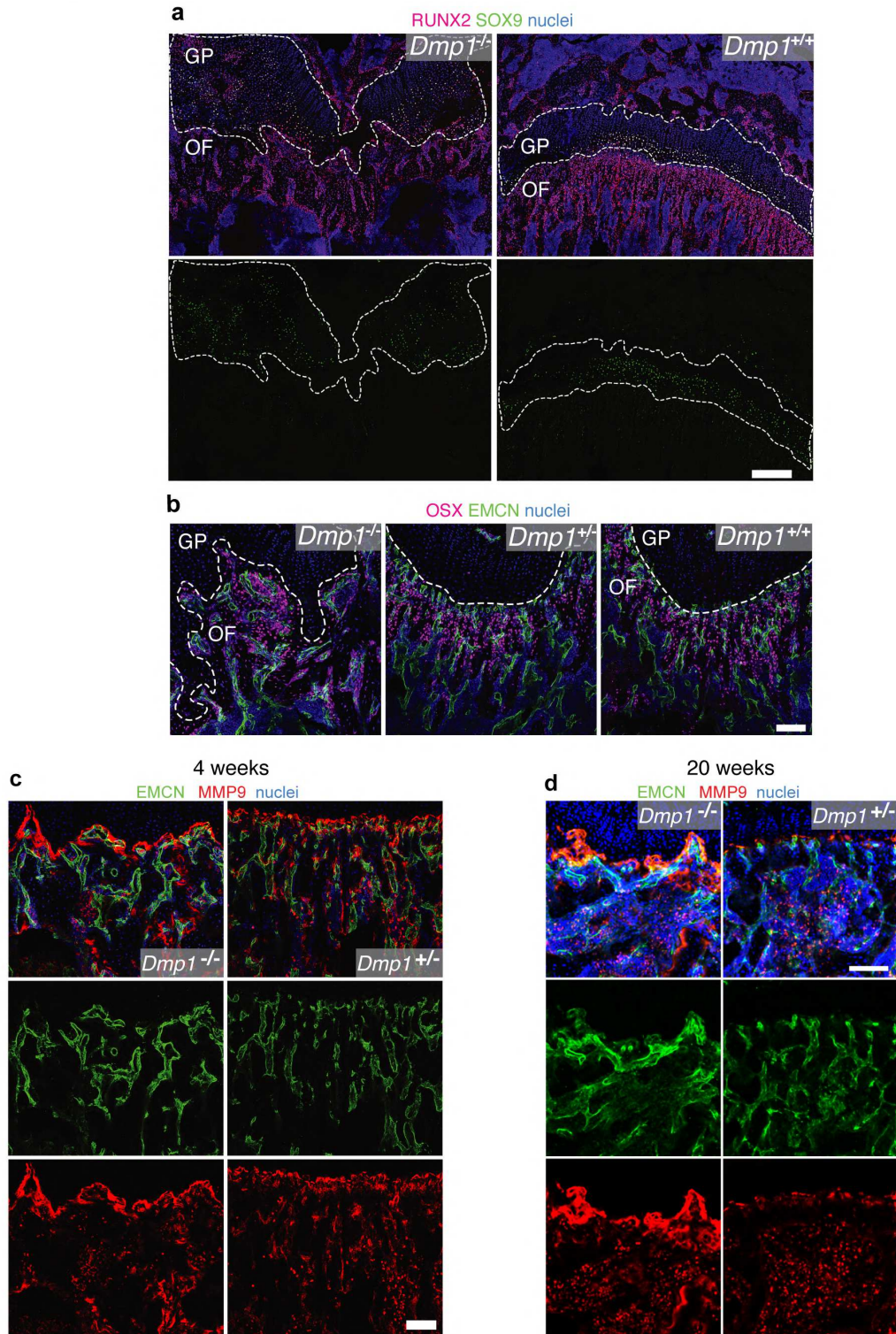


1  
2 **Extended Data Fig. 3: Identification of bulges and loss of type H vessels starting from 5.5-6 weeks of age**  
3 **in the centre of the ossification front.** **a**, EMCN and MMP9 immunostaining with a separated nuclei channel  
4 (Hoechst, left panel), which was used to define the border (dashed line) between OF and GP, based on cell density.  
5 This border then was copied to the respective full-colour image (right panel) to identify the bulges in the GP in an  
6 unbiased way. Scale bar 50  $\mu$ m. **b**, Quantification of EMCN intensity in the centre and periphery of the OF at  
7 different ages with a depiction of individual values per mouse in pairs. EMCN brightness decreases with ageing.  
8 At 4 and 5 weeks n=7, 5.5-6 weeks n=12, 8 weeks n=6, 12-15 weeks n=6. Pooled data from 6 independent  
9 experiments. Two-tailed paired *t*-test.  
10

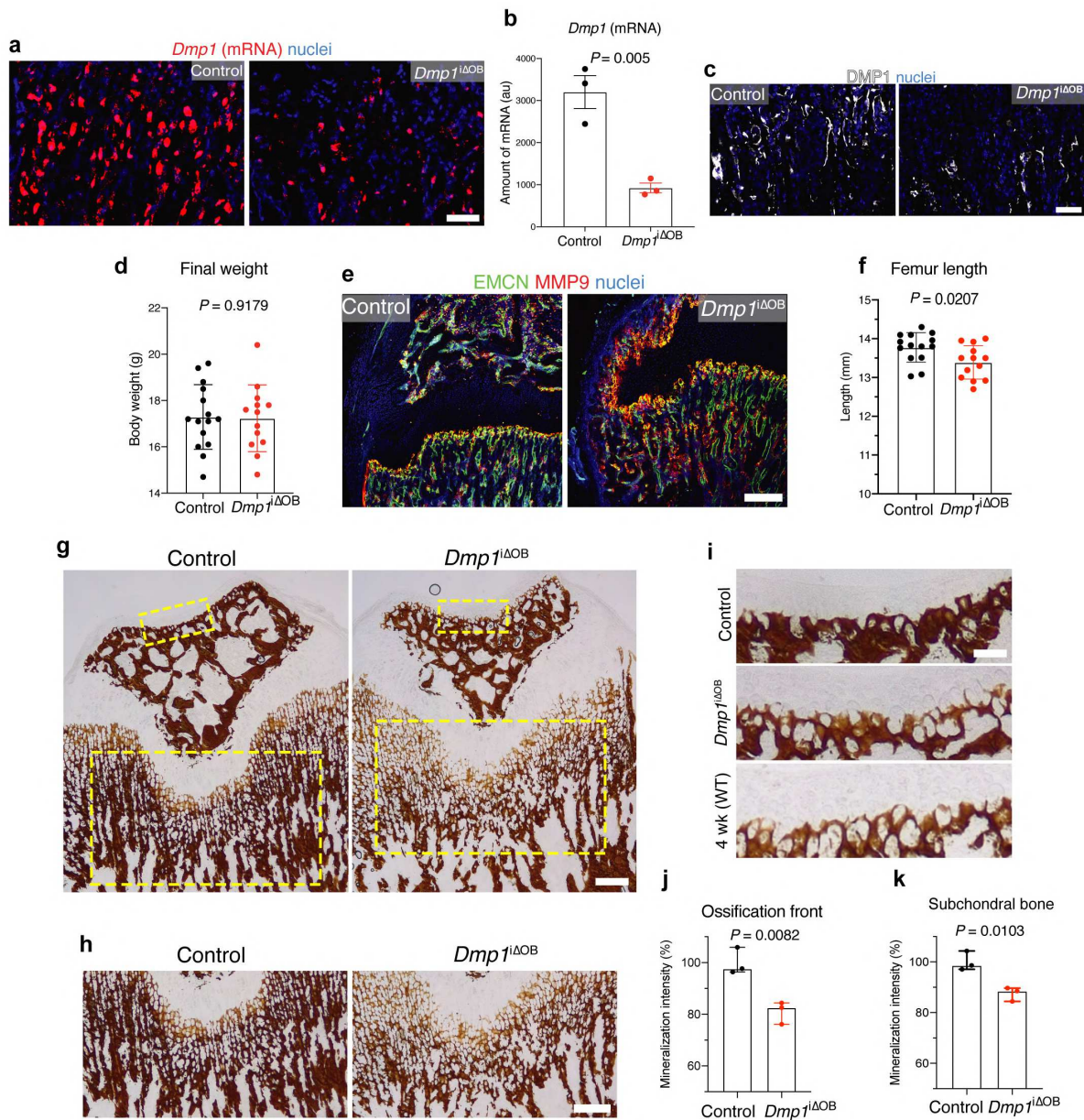


1  
 2 **Extended Data Fig. 4: Generation of *Dmp1*-deficient and *Dmp1*-floxed mice.** **a**, Scheme showing the wild-type  
 3 (top) and knockout version (bottom) of the *Dmp1* gene. Exon 6, encoding 80% of the protein, was cut out using  
 4 Crispr/Cas9 technology. The cutting was done 500bp upstream of Exon 6 and 500bp downstream of the open  
 5 reading frame (ORF), and the whole intermediate region was removed. **b**, PCR bands of the *Dmp1* gene in *Dmp1*-  
 6 *-/-*, *Dmp1*<sup>+/-</sup> and *Dmp1*<sup>+/+</sup> mice, where the band at ≈3800bp indicates the WT allele and at ≈1100bp the *Dmp1*-

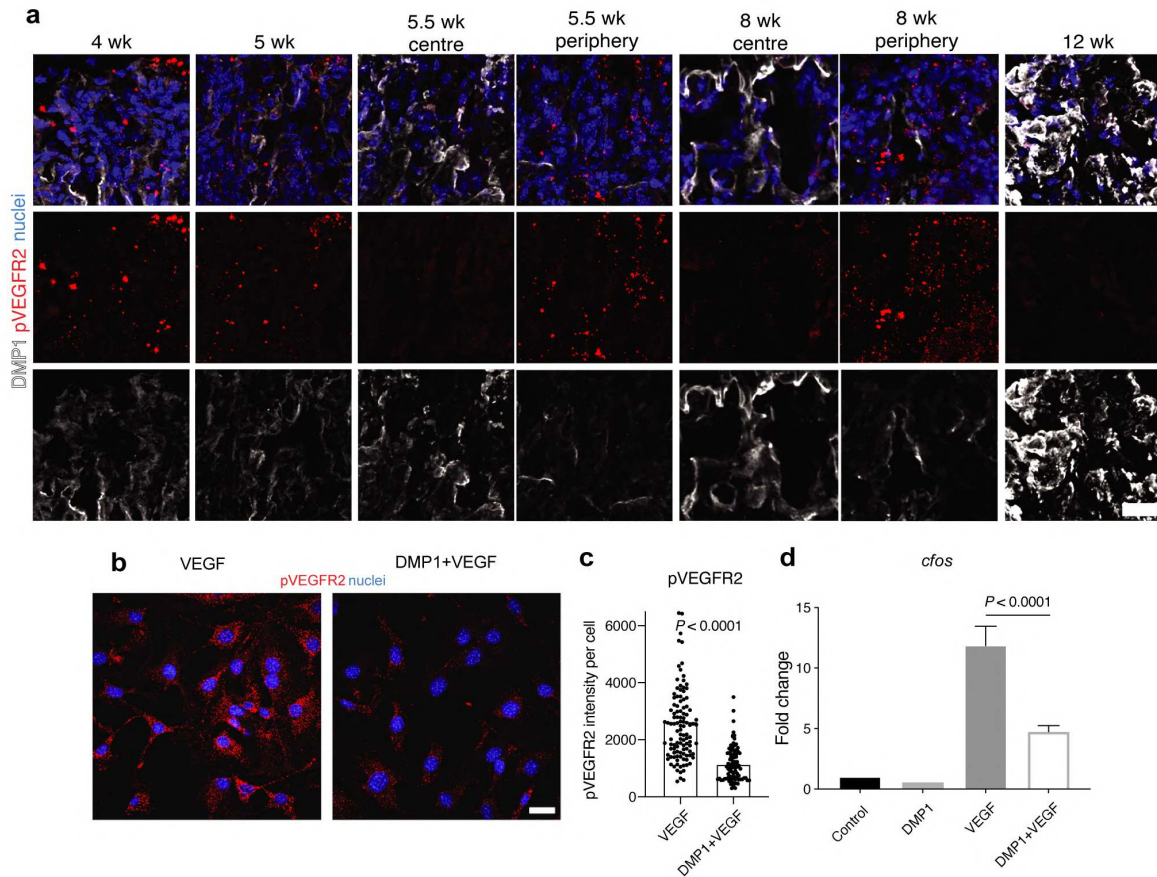
1 deficient variant. Note that the wild-type band in *Dmp1<sup>+/-</sup>* mice is very faint because of the PCR competition with  
2 the significantly smaller knockout allele. **c,d**, Body weight (**c**) and femur length (**d**) of *Dmp1<sup>-/-</sup>*, *Dmp1<sup>+/-</sup>* and *Dmp1<sup>+/+</sup>*  
3 mice at the age of 4.5-5 weeks. *P* values indicate the significance between *Dmp1<sup>-/-</sup>* versus *Dmp1<sup>+/-</sup>* and *Dmp1<sup>+/+</sup>*  
4 mice. Two-tailed *t*-test. **e**, Representative photo of *Dmp1<sup>-/-</sup>* and *Dmp1<sup>+/+</sup>* mice at the age of 15 weeks. **f**,  
5 Representative photo of *Dmp1<sup>-/-</sup>* and *Dmp1<sup>+/+</sup>* femurs at the age of 5 months. **g**, Scheme showing the wild-type  
6 (top) and floxed version of the *Dmp1* gene. LoxP sites were introduced 500bp upstream of Exon 6 and 500bp  
7 downstream of the ORF in the UTR region using Crisp/Cas9 technology. **h**, PCR bands of the *Dmp1* gene in  
8 *Dmp1<sup>fl/fl</sup>*, *Dmp1<sup>WT/fl</sup>* and *Dmp1<sup>WT/WT</sup>* mice showing that the introduced loxP sites make the allele 34bp longer than  
9 the WT version. **i**, PCR showing the appearance of the genomic *Dmp1*-knockout band only in cells from *Dmp1<sup>fl/fl</sup>*  
10 mice that were transduced with a Cre-recombinase encoding retrovirus.



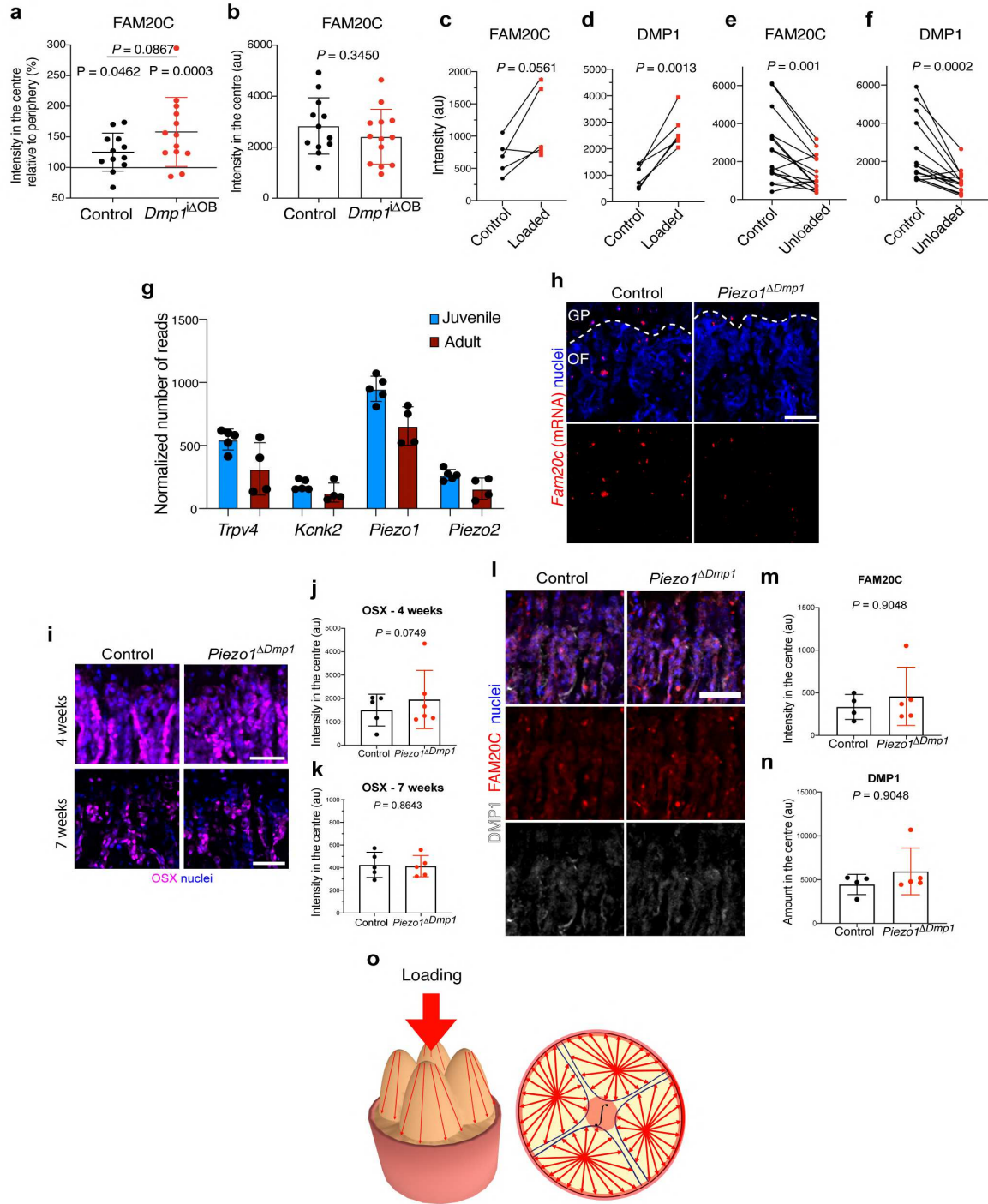
1  
 2 **Extended Data Fig. 5: DMP1-deficient mice exhibit very high EMCN and MMP9 intensity and the growth**  
 3 **plate is expanded and disorganised with enlarged SOX9 and RUNX2 zones. a,** RUNX2 and SOX9  
 4 immunostaining of metaphysis from 4.5-week-old *Dmp1*<sup>-/-</sup> and *Dmp1*<sup>+/+</sup> mice. Scale bar 250 μm. **b,** OSX and EMCN  
 5 immunostaining of femurs from 4.5-week-old *Dmp1*<sup>-/-</sup>, *Dmp1*<sup>+/-</sup> and *Dmp1*<sup>+/+</sup> mice from one litter. Scale bar 100 μm.  
 6 **c,d,** EMCN and MMP9 immunostaining of 4-week-old (c) and 20-week-old (d) femurs of *Dmp1*<sup>-/-</sup> and *Dmp1*<sup>+/-</sup> mice  
 7 from one litter. Scale bar 100 μm (c) and 200 μm (d).



1  
 2 **Extended Data Fig. 6: Osteoblast-specific *Dmp1* deletion preserves type H vessel identity and impairs bone**  
 3 **mineralization.** **a**, Representative *Dmp1* RNAScope images of control and *Dmp1*<sup>ΔOB</sup> OF. Scale bar 50 μm. **b**,  
 4 Quantification of *Dmp1* mRNA based on RNAScope images of control and *Dmp1*<sup>ΔOB</sup> mice at 6 weeks. 3 samples  
 5 per group were randomly selected, out of 14 and 13, respectively, for control and *Dmp1*<sup>ΔOB</sup> groups, to determine  
 6 the deletion efficiency. Two-tailed unpaired *t*-test. Mean ± SD. **c**, DMP1 immunostaining of OF in 6-week-old control  
 7 and *Dmp1*<sup>ΔOB</sup> femurs. Scale bar 50 μm. **d**, Body weight of control and *Dmp1*<sup>ΔOB</sup> mice at 6 weeks (P42). **e**, EMCN  
 8 and MMP9 immunostaining of 6-week-old control and *Dmp1*<sup>ΔOB</sup> femurs. Scale bar 250 μm. **f**, Femur length of  
 9 control and *Dmp1*<sup>ΔOB</sup> mice at 6 weeks (P42). **d,f**, Pooled data from 3 independent experiments. Control n=14,  
 10 *Dmp1*<sup>ΔOB</sup> n=13. Two-tailed unpaired *t*-test. Mean ± SD. **g**, Overview of von Kossa staining of undecalcified control  
 11 and *Dmp1*<sup>ΔOB</sup> femur sections. Yellow dashed rectangles indicate the regions shown in Extended Data Fig. 6h and  
 12 6i, and quantified in Extended Data Fig. 6j and 6k, respectively. Scale bar 200 μm. **h**, Von Kossa staining of  
 13 undecalcified control and *Dmp1*<sup>ΔOB</sup> femur sections (ossification front). Scale bar 200 μm. **i**, Von Kossa staining of  
 14 undecalcified control and *Dmp1*<sup>ΔOB</sup> femur sections (subchondral bone – articular cartilage area). Scale bar 50 μm.  
 15 **j,k**, Quantification of mineralization rate in the ossification front (**j**) and subchondral bone (**k**) by measuring the von  
 16 Kossa staining intensity in control and *Dmp1*<sup>ΔOB</sup> femurs. Age = 6 weeks. Control n=3, *Dmp1*<sup>ΔOB</sup> n=3. Two-tailed  
 17 unpaired *t*-test. Median ± range.



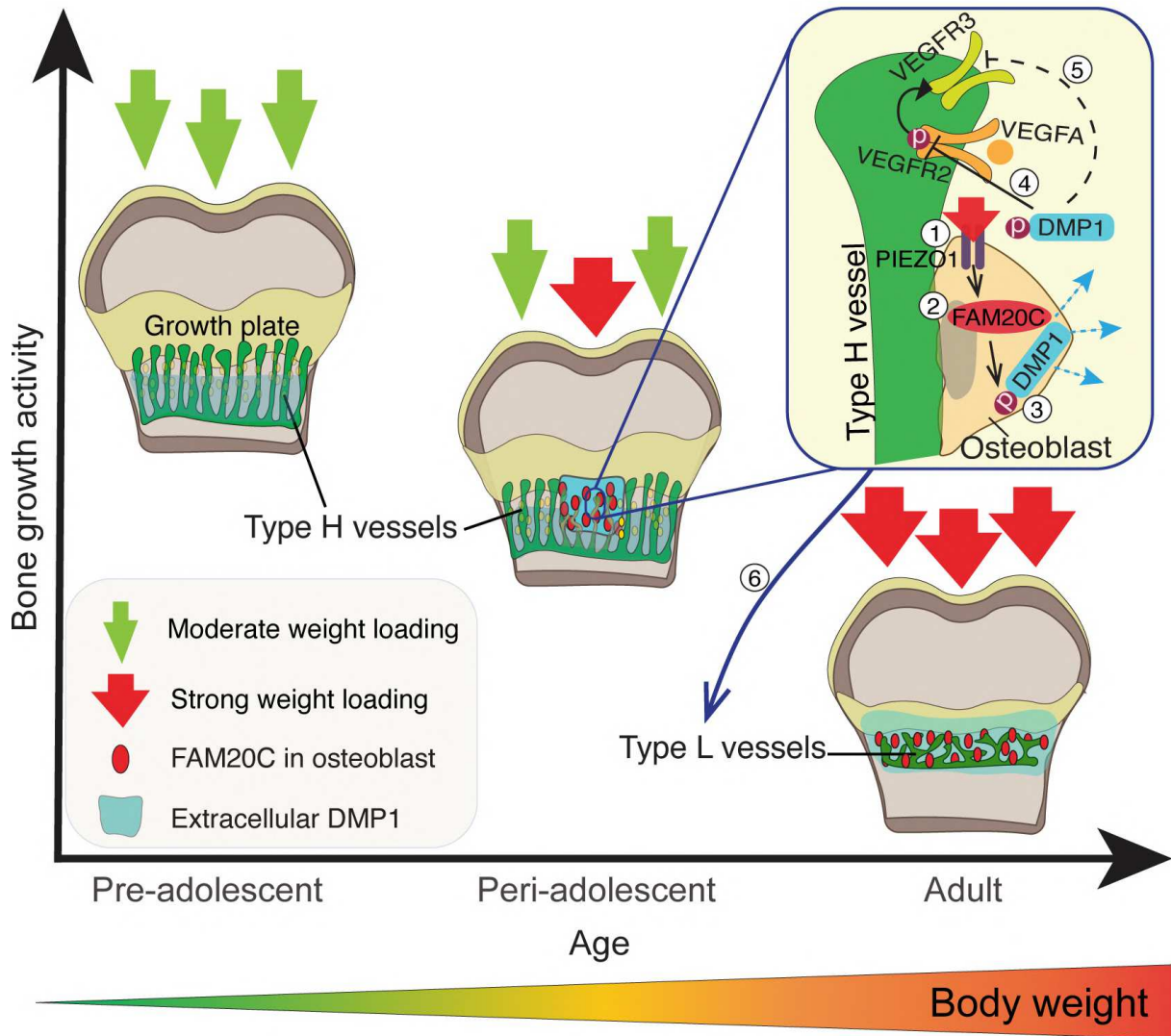
1  
2 **Extended Data Fig. 7: DMP1 abundance negatively correlates with the activation of VEGFR2 in the**  
3 **ossification front and DMP1 treatment inhibits VEGF signalling in endothelial cells *in vitro*.** **a**, DMP1 and  
4 phosphorylated VEGFR2 (pVEGFR2) immunostaining of the OF throughout postnatal development. Scale bar 50  
5  $\mu\text{m}$ . **b**, pVEGFR2 immunostaining of bEnd.3 cells, which were either treated with VEGF only (left) or pre-treated  
6 with DMP1 (40 nM) for 3 hours before adding VEGF (50 ng/ml). Scale bar 25  $\mu\text{m}$ . **c**, Quantification of the pVEGFR2  
7 intensity per cell of bEnd.3 cells, which were either treated with VEGF only or pre-treated with DMP1 before adding  
8 VEGF. Two-tailed Mann Whitney test. Mean. **d**, qPCR of *cfos* expression, one of the target genes of VEGF  
9 signalling, in bEnd.3 cells, which were treated either with DMP1 only, or with VEGF only, or first with DMP1 and  
10 then with VEGF. Tukey's multiple comparisons test. Mean  $\pm$  SD. **b-d**, Representative plots of 2 independent  
11 experiments.  
12



**Extended Data Fig. 8. Enhanced production of the DMP1-phosphorylating kinase FAM20C depends on mechanical forces sensed via PIEZO1 mechanoreceptor.** **a**, Quantification of the FAM20C amount in the centre relative to the periphery in the OF of femurs from 6-week-old control and  $Dmp1^{\Delta OB}$  mice. Top  $P$  value indicates the insignificance between control and  $Dmp1^{\Delta OB}$  groups. Bottom  $P$  values show the significance between the intensity in the centre versus periphery upon paired analysis for every mouse. Two-tailed paired  $t$ -test within a group. Two-tailed unpaired  $t$ -test between the groups. **b**, Quantification of the total FAM20C amount in the centre of the OF in the control and  $Dmp1^{\Delta OB}$  group. Two-tailed unpaired  $t$ -test. **a,b**, Pooled data from 3 independent experiments. Control  $n=12$ ,  $Dmp1^{\Delta OB}$   $n=13$ . Mean  $\pm$  SD. **c,d**, Quantification of the intensities of FAM20C (**c**) and DMP1 (**d**) in control and loaded (centrifuged) femur slice samples. Pooled data from 2 independent experiments.  $n=5-6$  (in one biological replicate staining for FAM20C was technically not possible due to the limited amount of material). Two-tailed paired  $t$ -test. **e,f**, Quantification of FAM20C (**e**) and DMP1 (**f**) intensities in loaded control (left) and unloaded (operated, right) femurs after double neurectomy. Pooled data from 2 independent experiments.  $n=16$ . Two-tailed Wilcoxon matched-pairs signed rank test. **g**, Normalized number of reads mapping to the genes of

1 mechanoreceptors expressed by endothelial cells together with surrounding cells in the juvenile and adult OF. Data  
2 are derived from the transcriptome analysis shown in Fig. 1 and Extended Data Fig. 1. **h**, Representative *Fam20c*  
3 RNAScope images of control and *Piezo1 $\Delta$ Dmp1* OF. Scale bar 50  $\mu$ m. **i**, OSX immunostaining of control and  
4 *Piezo1 $\Delta$ Dmp1* OF at 4 and 7 weeks of age. Scale bar 50  $\mu$ m. **j,k**, Quantification of OSX intensity in the OF of control  
5 and *Piezo1 $\Delta$ Dmp1* OF at 4 weeks (**j**) and 7 weeks (**k**) of age. Two-tailed unpaired *t*-test. Mean  $\pm$  SD. **l**, FAM20C and  
6 DMP1 immunostaining of 4-week-old control and *Piezo1 $\Delta$ Dmp1* ossification fronts. Scale bar 50  $\mu$ m. **m,n**,  
7 Quantification of FAM20C (**m**) and DMP1 (**n**) intensities in 4-week-old control and *Piezo1 $\Delta$ Dmp1* ossification fronts.  
8 Two-tailed unpaired *t*-test. Mean  $\pm$  SD. **o**, Schematic depiction of loading distribution (red arrows) in the growth  
9 plate in 3D (left) and in projection (right).  
10

# Molecular mechanism transforming type H into type L vessels to arrest adolescent bone growth



1  
2

3 Extended Data Fig. 9: Graphical abstract of the study.

## 1 **Materials and Methods**

### 2 Mice

3 *Tie2*-GFP reporter mice (Tg(TIE2GFP)287Sato/J, Stock No: 003658) were purchased from Jackson  
4 Laboratory. For analysis of wild-type femurs, C57BL/6N and C57BL/6J mice were used. C57BL/6J  
5 mice were used for double neurectomy experiments. *Dmp1*<sup>-/-</sup> and *Dmp1*<sup>fl/fl</sup> mice were produced by  
6 microinjection of C57BL/6J zygotes with Cas9 protein and synthetic guide RNA gDMP#1  
7 (TTGGGAAGATAACCGCTTAG) and gDMP#2 (CAGCTGAGGCGAGTACCACA). Thereby Exon  
8 6, which encodes 80% of the DMP1 protein, was deleted to generate constitutive *Dmp1*-deficient mice  
9 (Extended Data Fig. 4). For inducible deletion of *Dmp1*, loxP sites were inserted at the site of the gRNA  
10 target sites flanking Exon 6 using a customized gene targeting vector: 500 bp upstream of Exon 6 and  
11 500 bp downstream of the open reading frame (ORF). *Dmp1*-floxed mice were bred with *Colla2*-  
12 *CreERT2* mice, which were kindly provided by Prof. Dr. Thomas Blankenstein (Charité, Berlin). To  
13 induce Cre activity and gene deletion, 4-week-old offspring was injected intraperitoneally with 50  
14 mg/kg of tamoxifen (Sigma, T5648) for 5 consecutive days: P28-32. The resulting *Dmp1*<sup>iΔOB</sup>  
15 (*CreERT2*<sup>+/+</sup>*Dmp1*<sup>fl/fl</sup>) mutants and control (*CreERT2*<sup>-/-</sup>*Dmp1*<sup>fl/fl</sup>) mice were sacrificed on day P42 (6  
16 weeks) and the bones were collected for analysis. *Piezo1*<sup>fl/fl</sup>-*Dmp1Cre* and *Piezo2*<sup>fl/fl</sup>-*Dmp1Cre* were  
17 described before<sup>28</sup>. *Cre*-negative littermates were always used as controls.

18 In all experiments, both genders were analysed together and no gender-specific differences were  
19 observed. All mice were bred under specific pathogen-free (SPF) conditions and treated according to  
20 the requirements of the German legislation. Mice were kept in approved animal-care facilities and were  
21 housed 4-5 per cage in standard individually ventilated cages, maintained with a 12h light/dark cycle at  
22 an ambient temperature of 21°C. All animal experiments were performed according to relevant laws  
23 and institutional guidelines and were approved by local animal ethics committees (LAGeSo license  
24 number G0175/19).

### 25 Laser microdissection

26 *Tie2*-GFP mice were sacrificed via cervical dislocation at 4 weeks or 12 weeks of postnatal  
27 development. Femurs were immediately collected and frozen in SCEM medium using dry ice-

1 isopropanol-hexane cooling bath. After freezing the blocks were kept at  $-80^{\circ}\text{C}$  until cryosectioning.  
2 The temperature of the cryostat chamber and the knife was  $-32^{\circ}\text{C}$  and  $-34^{\circ}\text{C}$ , respectively. For  
3 cryosectioning, type D knife for hard tissue was used. All surfaces including the knife were cleaned  
4 with RNaseZap before use. Cryosectioning was performed with Kawamoto's films for LMD. To  
5 minimize RNA degradation,  $12\ \mu\text{m}$  sections were mounted into the metal frame directly after cutting  
6 and transported in the evaporating phase of liquid nitrogen. Laser microdissection was performed using  
7 Leica LMD7 device with fluorescent lamp for endothelial cell identification. To minimize the humidity  
8 during microdissection, constant flow of evaporating liquid nitrogen was applied. The microdissected  
9 pieces were collected into lysis buffer (ARCTURUS® PicoPure® RNA Isolation Kit). Approximately  
10 50 pieces were collected from each sample. Immediately after collection, the Eppendorf tube containing  
11 the sample was briefly centrifuged and incubated at  $42^{\circ}\text{C}$  for 10 min. Afterwards, it was vortex shortly  
12 and frozen on dry ice and kept at  $-80^{\circ}\text{C}$  until RNA isolation.

### 13 RNA sequencing and analysis

14 RNA was isolated using ARCTURUS® PicoPure® RNA Isolation Kit according to manufacturer's  
15 instructions. Illumina libraries were generated using SMART-Seq v4 Ultra Low Input RNA Kit (Takara  
16 Clontech) and Nextera XT DNA Sample Preparation Kit (Illumina), with up to 10 ng of purified cDNA.  
17 The quality of synthesized cDNA was checked using Bioanalyzer (Agilent). For sequencing, Illumina  
18 NextSeq500 device was used generating 75 bp paired-end reads. Reads were mapped to the mouse  
19 mm10 genome using TopHat2 (PMID: 23618408) and Bowtie2 (PMID: 22388286) with default  
20 settings<sup>46</sup>. Further analysis was done with R 3.4.0 using the default settings of the *deseq2* package  
21 (PMID:25516281). To identify the genes with the highest significance, fold change and decent  
22 expression level, the following filtering strategy was applied: mean expression value  $>500$ ,  $\text{Log}_2\ \text{FC} >$   
23  $0.66$ ,  $P < 10^{-5}$ . The heat map for selected genes was generated by plotting  $\text{log}_2$ -transformed read counts.

### 24 Immunohistochemistry

25 Mouse bones were processed as described previously<sup>47</sup>. Briefly, the bones were collected, cleaned from  
26 surrounding tissue and muscles, and immediately fixed in 4% freshly prepared ice-cold  
27 paraformaldehyde (PFA) for 4 h on ice. Afterwards, the bones were washed 3 times in ice-cold PBS

1 followed by decalcification in 0.5M EDTA solution (pH=7.5) for 24 h under constant agitation at 4°C.  
2 Cryoprotection was done overnight in 20% sucrose and 2% PVP solution at 4°C immediately after  
3 decalcification. Afterwards, 5 ml of embedding medium (8% gelatine, 20% sucrose and 2% PVP in  
4 PBS) was added per falcon tube and the bones were incubated in it for 45 min at 60°C followed by  
5 embedding into cryomolds. The femurs were always oriented the same way with the anterior side facing  
6 the bottom of the mould. After embedding the samples were left at room temperature (RT) for 30 min  
7 for complete medium solidification. The blocks were kept at -80°C in air-tight containers until  
8 cryosectioning. Cryosectioning was performed using NX70 ThermoFischer cryostat at -25°C and -27°C  
9 for chamber and blade, respectively. The disposable low-profile blades N35 for hard tissue (207500006,  
10 Feather) were used for cutting. 100 µm sections were generated and transferred onto Superfrost slides  
11 (J1800AMNT, Thermo Fisher Scientific). The slides were kept at -20°C until staining. For  
12 immunostaining, bone sections were air-dried, permeabilized in 0.3% Triton X-100 for 15 min, blocked  
13 in 10% donkey serum at RT for 30 min, and incubated with the primary antibodies diluted in 5% donkey  
14 serum in PBS for 2 h at RT or overnight at 4°C. After primary antibody incubation, sections were  
15 washed with PBS three times and incubated with corresponding secondary antibodies for 1 h at RT.  
16 Nuclei were counterstained with Hoechst (1:1000, 33342, Thermo Fisher Scientific). After incubation  
17 with secondary antibodies, sections were washed three times with PBS and mounted with Fluoromount-  
18 G medium (00-4958-02, Thermo Fisher Scientific).

### 19 RNAScope

20 Freshly dissected mouse femurs were fixed in 4% freshly prepared PFA for 24 h at 4°C followed by  
21 washings in PBS. Cryoprotection was performed via overnight incubations in 10, 20 and 30% sucrose  
22 at 4°C. Bones were frozen in SCEM medium. The frozen blocks were kept at -80°C until  
23 cryosectioning. Kawamoto cryofilms type 3C(16UF) were used for cryosectioning. The sections were  
24 air-dried in the cryotome for 15 min and stored at -80°C in the slide box with molecular sieves inside.  
25 For RNAScope assay, sections were air-dried at RT for 5 min, washed in PBS for 5 min and baked on  
26 60°C hot plate for 30 min followed by additional fixation in 4% PFA at 4°C for 15 min. Afterwards,  
27 the sections underwent 5 min dehydration steps in ethanol gradient: 50, 70 and 100% (x2). The sections  
28 were air-dried again for 5 min followed by 10 min incubation in hydrogen peroxide and washings in

1 distilled water. The target retrieval buffer was prewarmed in the steamer for ~10 min up to 75°C. The  
2 slides were submerged into it and left in the steamer for 10 min. The temperature in the steamer was  
3 95°C. Afterwards, the slides were washed in distilled water and dehydrated in 100% ethanol for 10-15  
4 sec. The slides were air-dried for 5 min at RT or overnight. Protease III was applied, and the slides were  
5 incubated in the HybeZ Oven for 30 min followed by washings in distilled water. The rest of the  
6 RNAScope procedure was performed according to the standard RNAScope® Multiplex Fluorescent v2  
7 Assay protocol.

#### 8 Double neurectomy

9 Mice received pre-emptive pre-operative subcutaneous analgesia. 5 mm pieces of sciatic and femoral  
10 nerves of the right hind limb were cut out in 4-4.5-week-old C57BL/6J mice under general anaesthesia  
11 using isoflurane. After surgery, the mice were housed without tubes and on soft bedding. It was  
12 observed that all mice dragged the operated right limb without stepping on it. Mice were sacrificed at  
13 the age of 5.5-6 weeks and the bones were collected for further analysis. The contralateral left femur  
14 was always used as control and was analysed in pair with the operated unloaded right femur.

#### 15 In vitro culture of bone slices

16 Femurs were collected from 4-week-old C57BL/6J mice. Half of the bone together with knee  
17 metaphysis was cut and frozen in 2.5% agarose on ice with subsequent cooling in liquid nitrogen. Under  
18 the sterile work bench, the frozen block was fixed on the sample holder for cryosectioning, which was  
19 placed on dry ice. 400-500 µm-thick slices of femur were produced using sterile disposable blade for  
20 hard tissue. Every slice was placed into a well of a 96-well PRC plate filled with StemMACS™  
21 OsteoDiff Media (Miltenyi Biotec). The position of the slice is depicted in Fig. 4a. At least two slices  
22 per femur were generated, each of them was placed into a separate plate. The plates were kept at 37°C  
23 with 5% CO<sub>2</sub> in a humidified atmosphere. One plate with slices was centrifuged twice daily at 19g (the  
24 lowest possible speed of the centrifuge) at 37°C for 30 min. The control plate was not subjected to  
25 centrifugation. The medium was changed every 2.5 days. After 5 days of culture, the slices were fixed  
26 in 4% PFA on ice for 30 min followed by washings in PBS and decalcification for 30 min in 0.5M  
27 EDTA on the cooling element under constant agitation. Cryoprotection was done in 20% sucrose and

1 2% PVP solution in PBS at 4°C overnight. The slices were frozen in embedding medium (8% gelatine,  
2 20% sucrose and 2% PVP in PBS). 100 µm sections were prepared using the NX70 Cryotome (Thermo  
3 Fischer Scientific). The sections were stored at -20°C until immunostaining. The staining was  
4 performed as described in the paragraph “Immunohistochemistry”. Paired analysis was done based on  
5 the slices derived from the same mouse.

#### 6 Image acquisition and analysis

7 All immunofluorescent and RNAScope-multifluorescent stainings were acquired at high resolution  
8 with Zeiss LSM-880 confocal microscope using 20x or 63x objectives. All microscope settings  
9 including laser power were kept constant throughout the experiments within the same type of samples  
10 and same staining panels. All immunostained samples were always acquired in Z-stack mode followed  
11 by maximum intensity projection. The images were processed and analysed using ImageJ and  
12 CellProfiler software, in compliance with *Nature*'s guide for digital images.

13 For quantification of immunofluorescent images, a region of 300µm width and 150µm depth (from the  
14 growth plate towards the caudal region) was always analysed. For RNAScope-multifluorescent images,  
15 the central and peripheral regions of 600µm x 300µm area underneath the growth plate were analysed.  
16 A cell was counted as *Runx2*<sup>+</sup> or *Osx*<sup>+</sup> if it contained at least one bright dot of the corresponding probe  
17 at 200x magnification.

#### 18 Endothelial cell culture

19 The mouse capillary endothelial cell line bEnd.3<sup>48</sup> was kindly provided by Prof. Dr. Alf Hamann  
20 (Charité, Berlin). The cells were cultured in ATCC-formulated Dulbecco's Modified Eagle's Medium  
21 (Catalogue No. 30-2002) containing 10% FCS and 100 U/mL penicillin and 100 mg/mL streptomycin.  
22 The cells were maintained at 37°C with 5% CO<sub>2</sub> in a humidified atmosphere. Cells were cultured with  
23 recombinant DMP1 (40 nM) for 4 or 24 h. At the end of this incubation time, VEGF (50ng/ml) was  
24 added to the cells for 15-20 min with subsequent cell fixation for immunocytochemistry or RNA  
25 collection for qPCR.

## 1 Immunocytochemistry

2 bEnd.3 cells were cultured in 8- or 16-well slide chambers (Tissue Tek). By the end of the experiment,  
3 cells were fixed in 4% freshly prepared ice-cold PFA for 10 min. Afterwards, they were washed 3 times  
4 with PBS and blocked in PBS containing 10% FCS for 30 min. The primary antibodies were applied  
5 for 1 h at RT in PBS containing 5% FCS and 0.1% Tween-20. After primary antibody incubation, cells  
6 were washed 3 times with PBS-Tween-20 (0.1%) and incubated with appropriate secondary antibodies  
7 diluted in PBS containing Hoechst (1:1000) for 1 h at RT. Finally, the cells were washed again 3 times  
8 with PBS and mounted using Fluoromount-G medium (Thermo Fischer Scientific).

## 9 qPCR

10 mRNA of bEnd.3 cells was isolated with the NucleoSpin RNA XS kit (Macherey Nagel) according to  
11 the manufacturer's protocol. cDNA was generated with TaqMan Reverse Transcription Reagents and  
12 quantified with PowerUp™ SYBR™ Green Master Mix using QuantStudio Real-Time PCR System  
13 (Thermo Fischer Scientific). The following primers were used: *Fos* (forward:  
14 CACTCCAAGCGGAGACAGAT, reverse: TCGGTGGGCTGCCAAAATAA), *Gapdh* (forward:  
15 AAGGTGATCCCAGAGCTGAA, reverse: CTGCTTACCACCTTCTTGA). *Fos* expression was  
16 normalized to *Gapdh*.

## 17 Von Kossa staining

18 The samples were prepared as described in paragraph "RNAScope". The staining was done according  
19 to the manufacturer's instructions (Silver plating kit acc. to von Kossa, Merck Millipore, #100362).  
20 Briefly, 10 µm undecalcified femur sections were placed in distilled water for 1 min followed by  
21 incubation in silver nitrate solution for 5 min under direct sunlight. Afterwards, the samples were  
22 washed in running tap water for 3 min and incubated in sodium thiosulfate solution for 5 min. Then the  
23 samples were washed in running tap water for 1 min and mounted in water-based mounting medium.  
24 The images were acquired with Leica DM750 equipped with Leica ICC50 W Camera Module using  
25 LAS software and analysed with ImageJ software (version 2.0.0).

1 Statistics

2 Statistical analysis was carried out using GraphPad Prism software (version 8.2). Normal distribution  
 3 was tested using Shapiro-Wilk and Kolmogorov-Smirnov tests. In case of normal distribution  
 4 parametric two-tailed paired *t*-test or unpaired *t*-test were used. For non-Gaussian distribution, non-  
 5 parametric tests were used: two-tailed Wilcoxon test for paired analysis and two-tailed Mann-Whitney  
 6 test for unpaired analysis.  $P < 0.05$  was considered significant. Mice with body weight that was >20%  
 7 below the average weight of their littermates were excluded from the inducible *Dmp1*-deletion  
 8 experiments. All image quantifications were done automatically upon manual blinded selection of  
 9 central and peripheral OF regions of the same size.

10

11 Primary antibodies

Name	Dilution	Catalogue number	Company
Endomucin (V.7C7)	1:100	sc-65495	Santa Cruz Biotechnology
DMP-1	1:100	AF4386	R&D systems
OSX (A-13)-R	1:200	sc-22536-R	Santa Cruz Biotechnology
MMP-9, biotin	1:200	BAF909	Novus
Integrin $\beta$ 3	1:100	4702S	Cell Signalling
FAM20C	1:100	25395-1-AP	Proteintech
RUNX2 [EPR14334] (Alexa Fluor® 647)	1:200	ab215955	Abcam
SOX9 [EPR14335] (Alexa Fluor® 594)	1:200	ab202517	Abcam
MCM-BP	1:100	ab122478	Abcam
PDGF R beta Biotinylated	1:100	BAF1042	R&D systems
Phospho-VEGF Receptor 2 (Tyr1175) (19A10)	1:100	2478S	Cell Signaling
VEGFR2/KDR/Flk-1	1:50	AF644	R&D systems
VEGFR3/Flt-4	1:50	AF743	R&D systems

12

## Secondary antibodies

Name	Dilution	Catalogue number	Company
Donkey anti-Rabbit IgG (H+L) Secondary Antibody, Alexa Fluor 555	1:500	A-31572	Thermo Fisher Scientific
Goat anti-Rabbit IgG (H+L) Secondary Antibody, DyLight 633	1:400	35562	Thermo Fisher Scientific
Donkey anti-Rabbit IgG (H+L) Secondary Antibody, Alexa Fluor® 594 conjugate	1:500	A-21207	Thermo Fisher Scientific
Donkey anti-Rabbit IgG (H+L) Cross-Adsorbed Secondary Antibody, DyLight 488	1:400	SA5-10038	Thermo Fisher Scientific
Donkey Anti-Sheep IgG NorthernLights™ NL493-conjugated Antibody	1:200	NL012	R&D systems
Donkey Anti-Sheep IgG NorthernLights™ NL637-conjugated Antibody	1:200	NL011	R&D systems
Donkey anti-Rat IgG (H+L) Cross Adsorbed Secondary Antibody, DyLight 488 conjugate	1:400	SA5-10026	Thermo Fisher Scientific
Donkey anti-Rat IgG (H+L) Cross Adsorbed Secondary Antibody, DyLight 550 conjugate	1:400	SA5-10027	Thermo Fisher Scientific
Donkey anti-Rat IgG (H+L) Cross-Adsorbed Secondary Antibody, DyLight 594	1:400	SA5-10028	Thermo Fisher Scientific
Donkey anti-Goat IgG (H+L) Alexa Fluor 633	1:500	A-21082	Thermo Fisher Scientific
Streptavidin AF-555	1:2000	S32355	Thermo Fisher Scientific

1  
2  
3

## Reagents

Name	Catalogue number	Company
Embedding medium SCEM	C-EM001	Section-Lab
2 propanol ≥99,5 %, Ph.Eur., reinst.	CP41.3	Carl Roth
n-Hexane	7339.1	Carl Roth

RNaseZap™ RNase Decontamination Solution	AM9780	Thermo Fisher Scientific
ARCTURUS® PicoPure® RNA Isolation Kit	KIT0204	Thermo Fisher Scientific
SMART-Seq v4 Ultra Low Input RNA Kit for Sequencing	634889	Takara-Clontech
Nextera XT DNA Sample Preparation Kit (Illumina)	FC-131-1024	Illumina
20% Paraformaldehyde (formaldehyde) aqueous solution	50-980-492	Science Services
Ethylenediaminetetraacetic acid disodium salt dihydrate	8043.3	Carl Roth
Polyvinylpyrrolidon K 90	CP15.1	Carl Roth
Gelatine	4274.3	Carl Roth
D(+)-Saccharose	4621.1	Carl Roth
Tissue Freezing Medium	14020108926	Leica biosystems
Triton x-100	93418	Fluka BioChemika
Tween-20	P1379	Sigma-Aldrich
Fluoromount-G mounting medium	00-4958-02	Thermo Fisher Scientific
ATCC-formulated Dulbecco's Modified Eagle's Medium	30-2002	ATCC
StemMACS™ OsteoDiff Media	130-091-67	Miltenyi Biotec
Tamoxifen	T5648-1G	Sigma-Aldrich
Recombinant mouse VEGF-A	493-MV-005	R&D systems
Recombinant mouse DMP1	4386-DM-050	R&D systems
Power SYBR Green Master Mix	4368708	Thermo Fisher Scientific
Taq Man cDNA polymerase	4304134	R&D systems
Hoechst 33342 Solution (20 mM)	62249	Thermo Fisher Scientific
Opal 570	FP1488001KT	Akoya Biosciences
Opal 620	FP1495001KT	Akoya Biosciences
Opal 650	FP1496001KT	Akoya Biosciences
Silver plating kit acc to von Kossa	100362	Merck Millipore

1

2 Consumables

3

Name	Catalogue number	Company
Cryomoulds	SA62534-15	Tissue-Tek
Kawamoto's LMD tape	C-FL001	Section-lab
Kawamoto's tape 3C(16UF)	C-FUF304	Section-lab
Thin-walled, frosted lid, RNase-free PCR tubes (0.2 mL)	AM12225	Thermo Fischer Scientific

Microtome Blade - N35 for hard tissue	207500006	Feather
Superfrost Plus slides	J1800AMNT	Thermo Fischer Scientific
Polysine slides	10219280	Thermo Fischer Scientific
Molecular sieves	8483	Carl Roth
Microtube tough-spots	N120.1	Carl Roth
Coverslips	LH24.1	Carl Roth
16-well Chamber Slide with removable wells	178599	Thermo Fischer Scientific

1

2

1 **Extended data references**

2  
3  
4  
5  
6  
7  
8  
9  
10  
11

46. Langmead, B. & Salzberg, S. L. Fast gapped-read alignment with Bowtie 2. *Nature Methods* **9**, 357–359 (2012).
47. Kusumbe, A. P., Ramasamy, S. K., Starsichova, A. & Adams, R. H. Sample preparation for high-resolution 3D confocal imaging of mouse skeletal tissue. *Nature Protocols* **10**, 1904–1914 (2015).
48. Sikorski, E. E., Hallmann, R., Berg, E. L. & Butcher, E. C. The Peyer’s patch high endothelial receptor for lymphocytes, the mucosal vascular addressin, is induced on a murine endothelial cell line by tumor necrosis factor-alpha and IL-1. *Journal of Immunology* **151**, 5239–5250 (1993).

# Figures

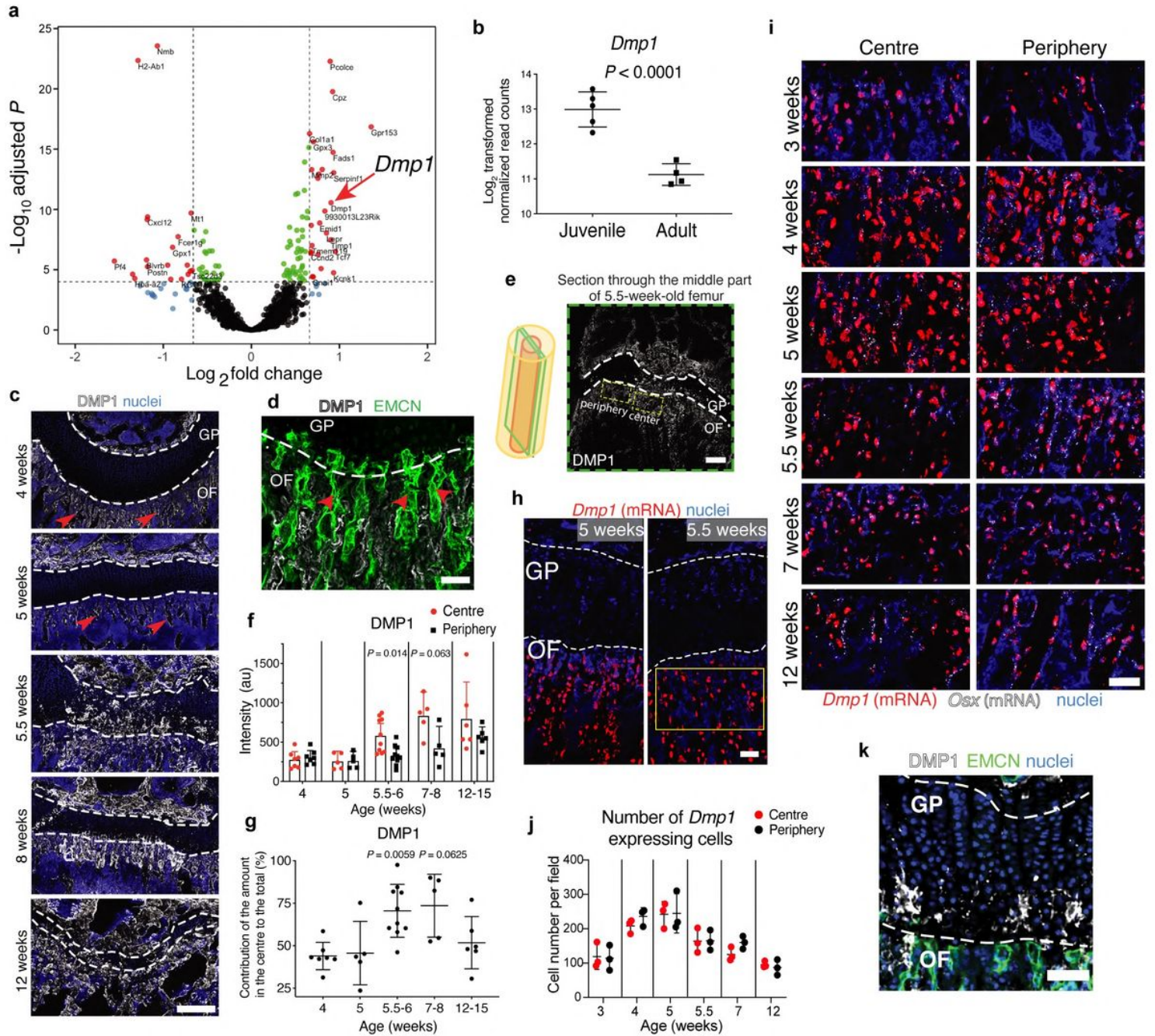


**Figure 1**

Burst in DMP1 secretion from osteoblasts into ECM at the OF-GP border during periadolescence. (see full caption in Manuscript file)

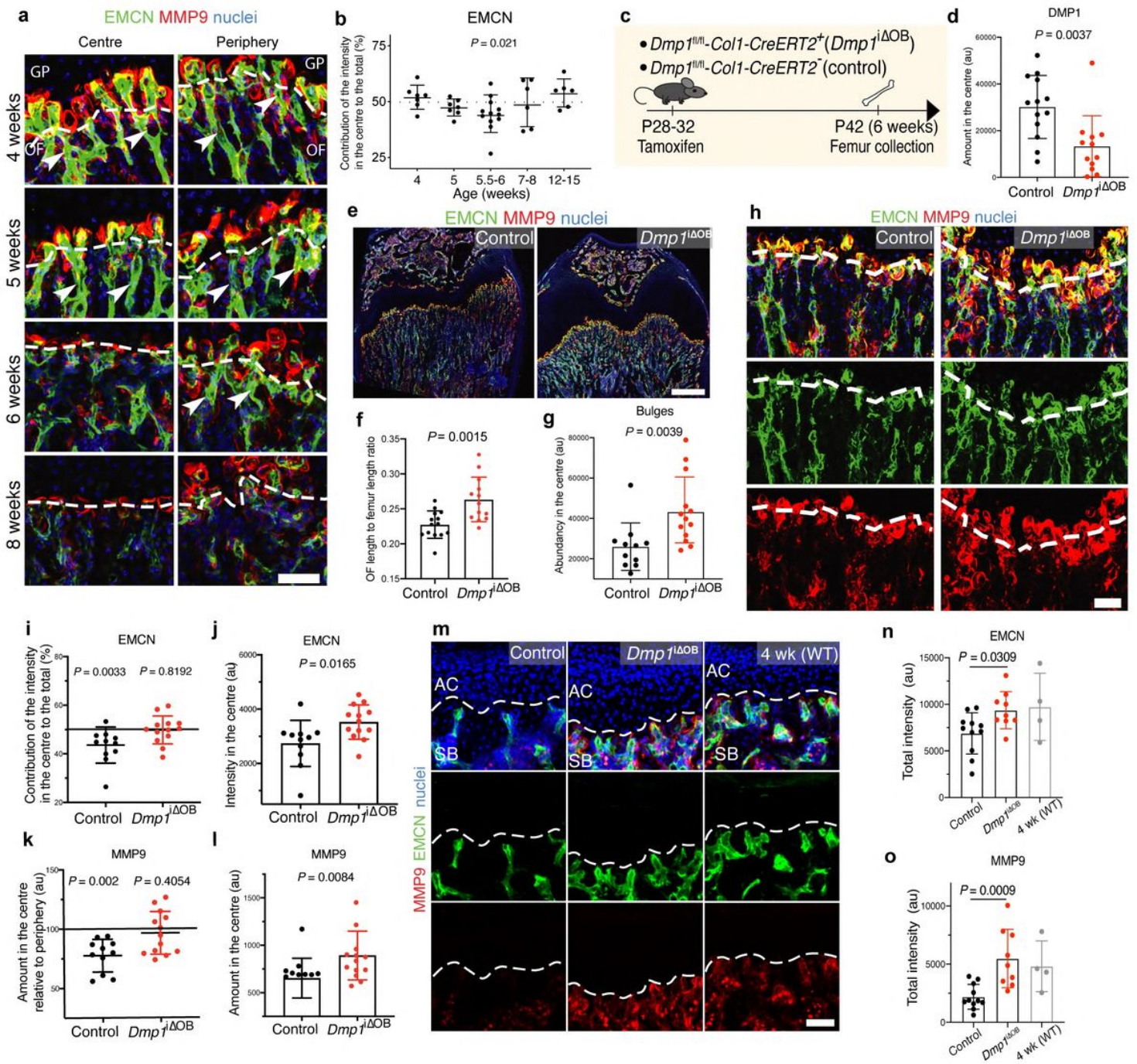


**Figure 2**

DMP1 transforms active type H vessels into quiescent type L in the ossification front and in subchondral bone.(see full caption in Manuscript file)

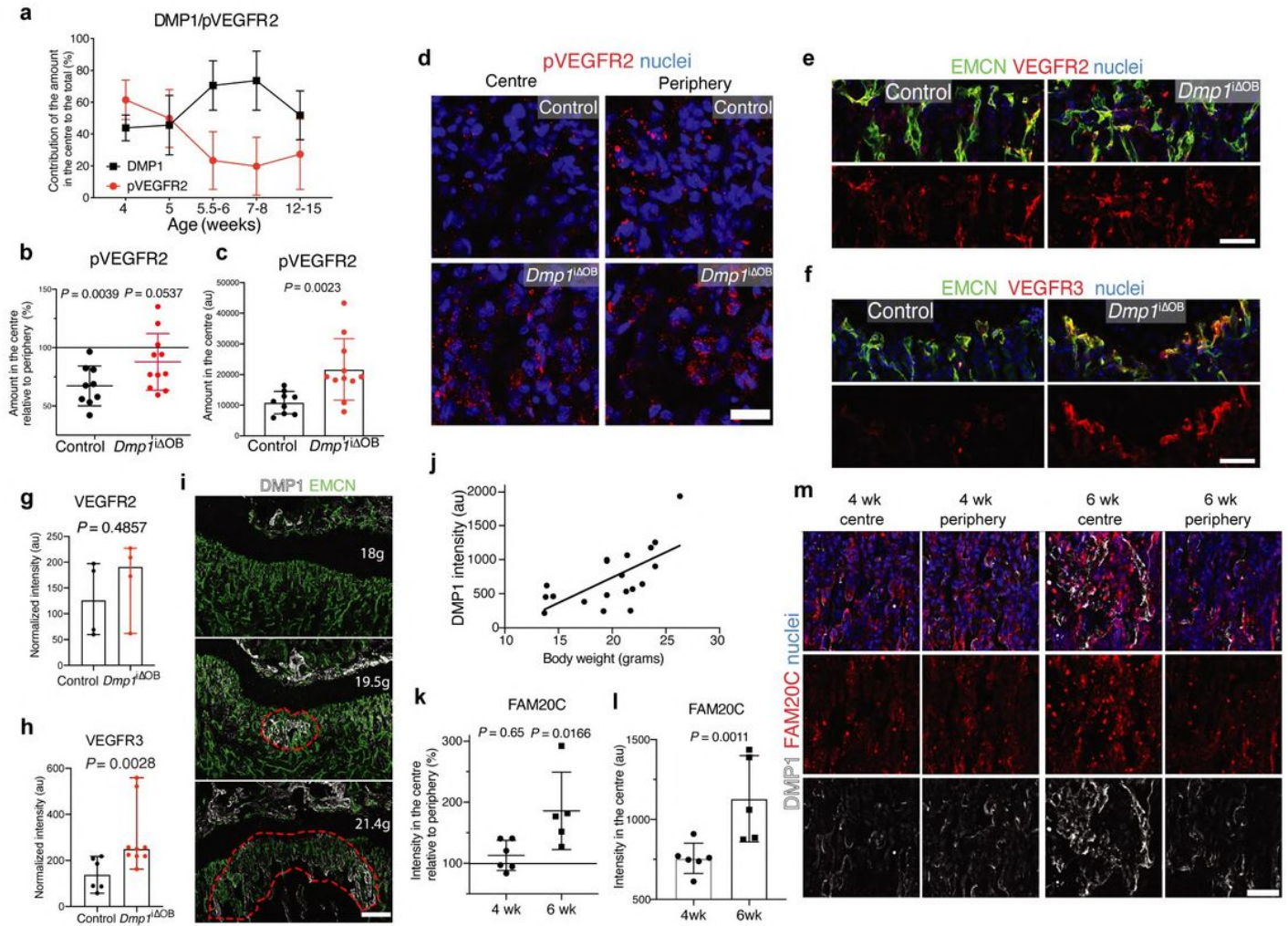


**Figure 3**

Extracellular DMP1 inhibits VEGF signalling in the OF and coincides spatiotemporally with FAM20C upregulation. (see full caption in Manuscript file)

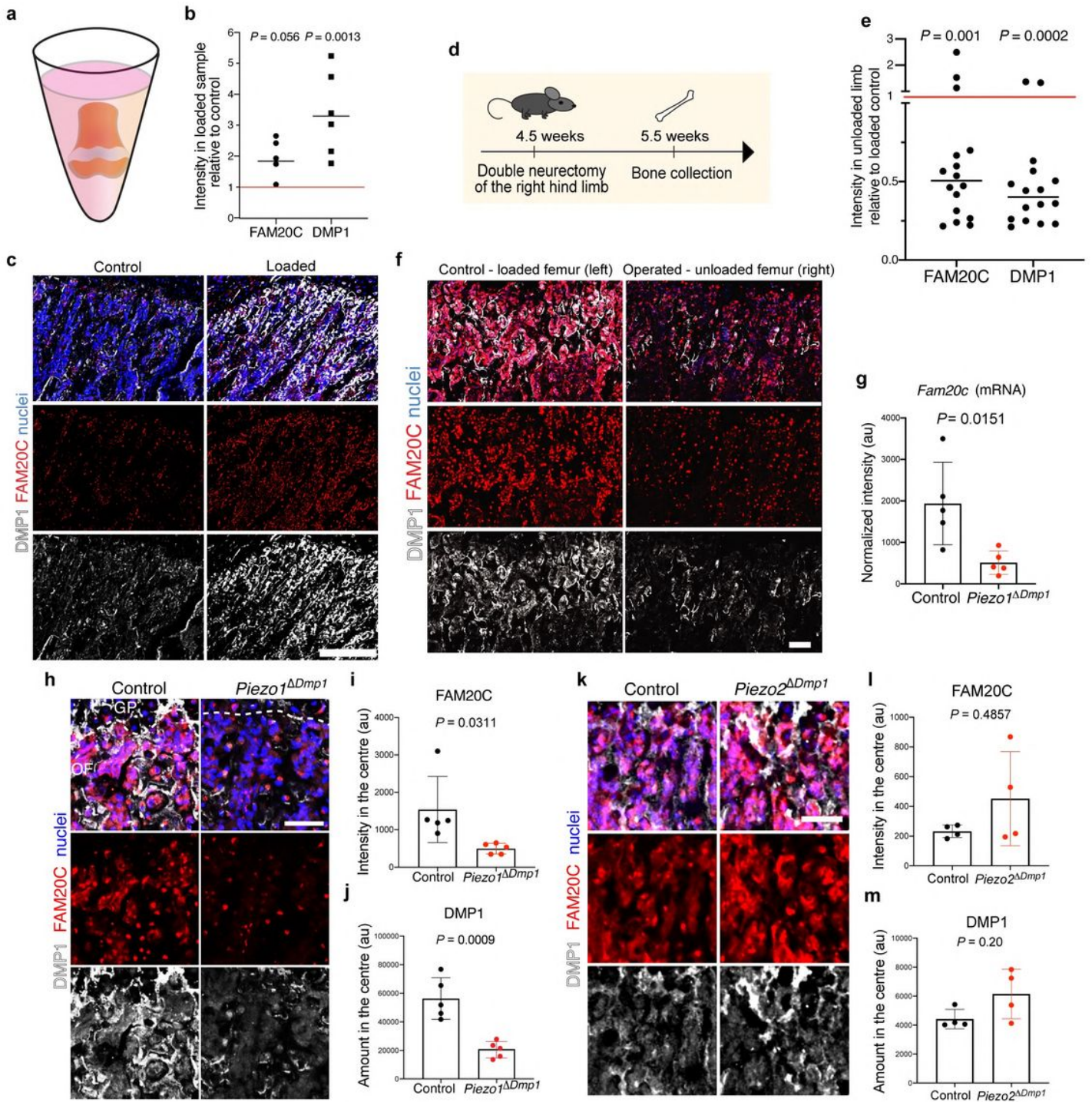


**Figure 4**

Mechanical forces trigger PIEZO1 to enhance FAM20C kinase production and DMP1 secretion. (see full caption in Manuscript file)